International Journal of Earth Sciences (2022) 111:1079–1106
https://doi.org/10.1007/s00531-021-02129-2

ORIGINAL PAPER

Chronology, geochemical characteristics, and tectonic implications of a Triassic complex in the Rongma Area, Southern Qiangtang, Tibet

Zheng-Zhe Fan[1] · Quan Wang[2] · Xian Chen[3] · Gen-Hou Wang[4] · Yue Fu[5] · Gui-Juan Guo[6]

Received: 28 October 2019 / Accepted: 28 October 2021 / Published online: 10 March 2022

Abstract

The spatio-temporal evolution of the Paleo-Tethys Ocean has been a hot and controversial issue in the world. Here we carry out petrographic, chronological, and geochemical study on garnet–phengite–quartz schist and mafic rocks in the Rongma area from the northern margin of the Southern Qiangtang block to determine the early Mesozoic tectonic evolution of the Shuanghu Paleo-Tethys Ocean in northern Tibet. The zircons from a phengite–quartz schist sample yielded concordant ages of 1936–393 Ma, indicating that its protolith deposited after ~ 393 Ma. Overgrowth zoning garnet with three stages of metamorphic evolution from garnet core to rim (i.e., Peak metamorphic, early retrograde metamorphic, and late retrograde metamorphic stages) in the schist was recognized, indicating that two subduction in a short time might be involved for its genesis. Two groups of phengite in the schist yielded $^{40}Ar/^{39}Ar$ plateau ages of 229 ± 1.4 Ma and 225 ± 1.3 Ma, respectively; thus, the late retrograde metamorphism of the schist might occur at ~ 229–225 Ma. Zircon U–Pb dating of a diabase in the area yielded crystallization age of 241 ± 1.1 Ma implying its formation in the early Triassic. The Hf-in-zircon and whole-rock Nd isotopes of the diabase show $\varepsilon_{Hf}(t)$ of − 0.6- + 19.1 and $\varepsilon_{Nd}(t)$ of − 0.8 to + 0.9, respectively. Combined with the whole-rock geochemical features of the early Triassic diabase (241 Ma) and gabbro (237 Ma), they indicate that these mafic rocks are formed in a back-arc extensional setting related to the subduction of the oceanic plate between the Northern and Southern Qiangtang blocks beneath the latter. Combined with regional data, our study favors that view bi-directional subduction of the Shuanghu Paleo-Tethys ocean in the Early Triassic and it was finally closed at ~ 237 to ~ 229 Ma. Our model will help us better understand the tectonic evolution of the Paleo-Tethys Ocean.

Keywords Southern Qiangtang block · Diabase · Garnet–phengite–quartz schist · Geochemistry · Metamorphic evolution

Introduction

The spatio-temporal evolution of the Paleo-Tethys Ocean has been a topic of debate for decades, for instance, the Shuanghu Paleo-Tethys in northern Tibet (e.g., Li 1987; Deng et al. 1996; Kapp et al. 2000; Li e al., 2008a, b, 2019; Pullen et al. 2008; Yin and Harrison 2000; Kapp et al. 2003; Zhang et al. 2006a, b, 2007, 2011, 2016, 2018; Zhang and Tang 2009). The LongmuTco–Shuanghu Suture Zone in the Tibet Plateau of western China runs through the hinterland of the Qiangtang Basin and separates it into northern and southern (or eastern and western) Qiangtang blocks (Fig. 1a). The suture zone is marked by the central Qiangtang metamorphic belt (CQMB) (Fig. 1b), including an assemblage of eclogites, eclogitic metasediments, metasedimentary schists and gneisses, and marble (e.g., Zhang et al. 2006a, b, 2012), which is key to understand the tectonic evolution of the Paleo-Tethyan realm and the crustal architecture of

✉ Quan Wang
wquan@mail.cgs.gov.cn

✉ Xian Chen
chenxian1@mail.gyig.ac.cn

1 School of Earth Sciences, Northeast Petroleum University, Daqing 163318, China

2 Development and Research Center, China Geological Survey, Beijing 100037, China

3 Institute of Geochemistry, Chinese Academy of Sciences, Guiyang 550081, China

4 School of Earth Sciences and Resources, China University of Geosciences (Beijing), Beijing 100083, China

5 Chemical Analysis and Detection Center, Construction and Design Research Institute of Daqing Oilfield, Daqing 163000, China

6 Seismological Press, Beijing, China

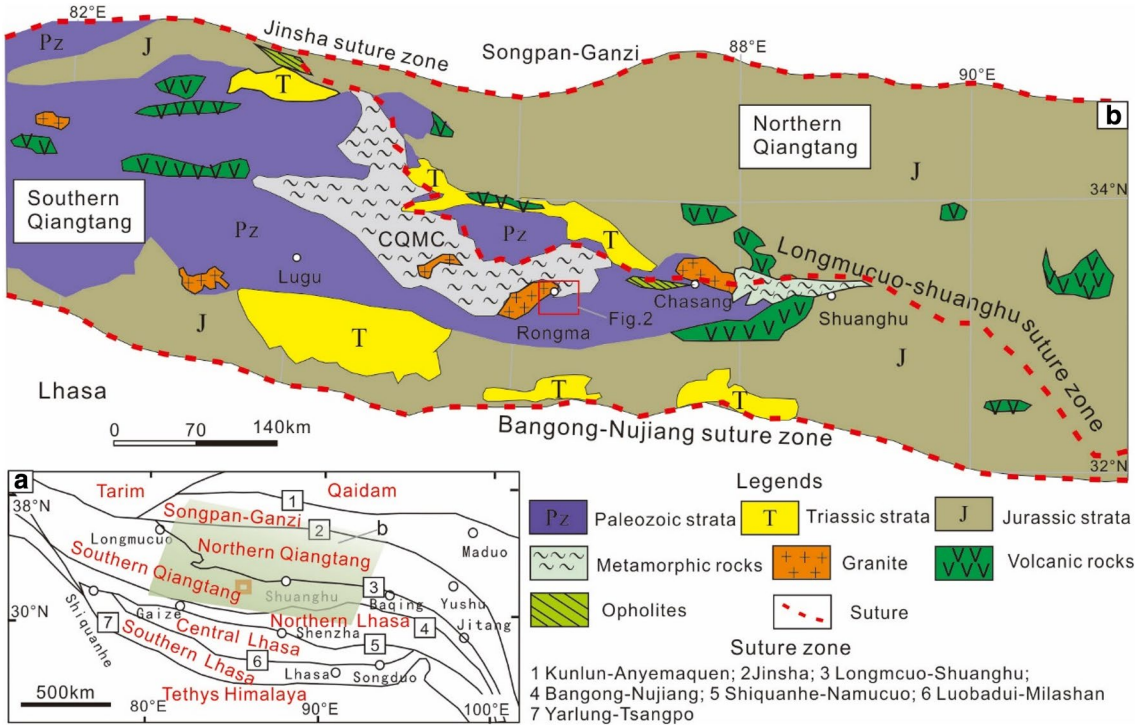

Fig. 1 **a** Simplified tectonic map of Tibet, western China; **b** simplified geological map of the central Qiangtang metamorphic belt (modified after Zhang et al. 2011)

the Tibetan plateau. Although at least three distinct models have been proposed to interpret the nature and origin of the CQMB: (i) a continental rift model (e.g., Deng et al. 1996); (ii) an allochthonous underthrust mélange model (Kapp et al. 2000, 2003); (iii) an in situ Paleo-Tethyan suture model (e.g., Zhang et al. 2006a, b), more and more evidences from abundant ophiolite slices (Li et al. 2008a, b; Wu 2013; Zhai et al. 2004, 2007; Zhang et al. 2016), low-temperature, high–ultra-high-pressure metamorphic complexes (Li et al. 2006; Zhai et al. 2011a, b; Zhang et al. 2006a, b, 2018), paleomagnetic and faunal–floral data (Lu et al. 2019), and widespread magmatism related to subduction and collision paralleled to the suture zone (e.g., Hu et al. 2014; Li et al. 2015a, b; Lu et al. 2017; Peng et al. 2015; Zhang et al. 2011) supported the third model, and i.e., the LongmuTco–Shuanghu suture zone most likely represents the remnant of the Paleo-Tethys Ocean and the nature and origin of CQMB are mainly constrained by the evolution of the Paleo-Tethys Ocean (e.g. Li et al. 2006; Zhang et al. 2006a 2006b 2011 2016 2018; Zhai et al. 2011a 2011b; Lu et al. 2019). Researchers have proposed the opening of this ocean in the Cambrian (e.g., Zhai et al. 2013) or the Devonian (Zhang et al. 2014a, b) by ophiolite studies and the closure in the Middle Triassic (e.g., Hu et al. 2014; Peng et al. 2015; Tao et al. 2014) or late Triassic (Wang et al. 2019) through granite data or after late Triassic based on metamorphic rock evidence (Zhang et al. 2018). Hence, the opening and closure time of the Shuanghu Paleo-Tethys Ocean remains controversial. In addition, whether bi-directional subduction of the Shuanghu Paleo-Tethys Ocean occurred during its evolution is also a topic of debate. Predominant studies insisted in a unidirectional subduction of the oceanic plate between the Southern and Northern Qiangtang blocks beneath the latter during the evolution of the Shuanghu Paleo-Tethys Ocean (e.g., Zhang et al. 2006a, b; Zhai et al. 2011a, b; Li et al. 2019). However, the other studies asserted that bi-directional subduction of the Shuanghu Paleo-Tethys Ocean occurred during its evolution (e.g., Liu et al. 2011; Zhao et al. 2015). Hence, it is necessary to further explore these issues.

Although ophiolite suites have provided a strong evidence for the existence of an ancient ocean, they are usually sporadically preserved during subduction and surface processes. Thus, the accurate evolution of the ocean cannot be constrained. The study on petrogenesis with integrated metamorphic and igneous rocks will give a proper avenue to determine the secular evolution of an ancient ocean (Zhou et al. 2009; Wu et al. 2011; Yu et al. 2012; Wilde and Zhou 2015; Zhu et al. 2015). Hence, here we carry out petrographic, chronological, and geochemical study on garnet–phengite–quartz schist and mafic rocks in the Rongma area, northern margin of the Southern Qiangtang block, to determine the metamorphic processes of the schist and the

petrogenesis of the mafic rocks and to further reveal the early Mesozoic tectonic evolution of the Shuanghu Paleo-Tethys Ocean in northern Tibet.

Regional geology

The Qinghai–Tibet Plateau consists of a series of tectonically splicing terranes, including the Qaidam, Songpan–Ganzi, Qiangtang, and Lhasa terranes, separated by several well-known sutures (Yin and Harrison, 2000; Zhang et al. 2012; Fig. 1a). The Qiangtang Basin is located in the northern margin of the Tibet Plateau and is separated into the southern and northern (or eastern and western) Qiangtang blocks by the LongmuTco–Shuanghu Suture Zone. The southern and northern Qiangtang blocks differ greatly in sedimentary strata and palaeontologic characteristics; the Southern Qiangtang block might have an affinity to the Gondwana, whereas the Northern Qiangtang block might have an affinity to the Yangtze plate in the Eurasia (Li et al. 2004, 2005). The study area is located in Yadan, Rongma Town, northern margin of the southern Qiangtang, and is geotectonically located ~ 80–100 km south of the LongmuTco–Shuanghu Suture Zone (Fig. 1a, b). Regional stratigraphy mainly comprises the late Plaeozoic–Cenozoic strata, such as the Devonian sandstone and siltstone, the Carboniferous–Permian limestone with sandstone, the Upper Triassic limestone with sandstone, the Upper Cretaceous conglomerate and sandstone, the Paleogene terrigenous clastic rocks, and the Quaternary terrigenous talus accumulations. Accreting complex and sedimentary cover zones widely occurred in the region (Wang et al. 2009). The accreting complexes contain argillaceous, quartz schist, marble, pillow basalt, gabbro and diabase, and so on, which have suffered from intense deformation, metamorphism, and feature disordered sequence (Liu et al. 2011); The sedimentary cover zone features intense deformation and weak metamorphism (Wang et al. 2009). Regional strike-slip fault is developed, displaying multi-staged metamorphism–deformation mainly with a NE–SW trending (Fig. 2a, b).

The late Plaeozoic, Mesozoic, and the Cenozoic igneous rocks widely occurred in the region (Wang et al. 2019). The late Paleozoic magmatic rocks are predominantly outcropped in the northwest, with the Mesozoic and the Cenozoic magmatic rocks mainly in the central area (Fig. 2a, b). Intrusive rocks include mafic dykes [e.g., sillite, gabbro, and diabase–gabbro, as well as granitoids (Fig. 2a, b)]. The mafic dykes were mainly formed in the late Carboniferous–early Triassic (Li et al. 2005; Zhai et al. 2009; Dan et al. 2020, 2021). Volcanic rocks mainly

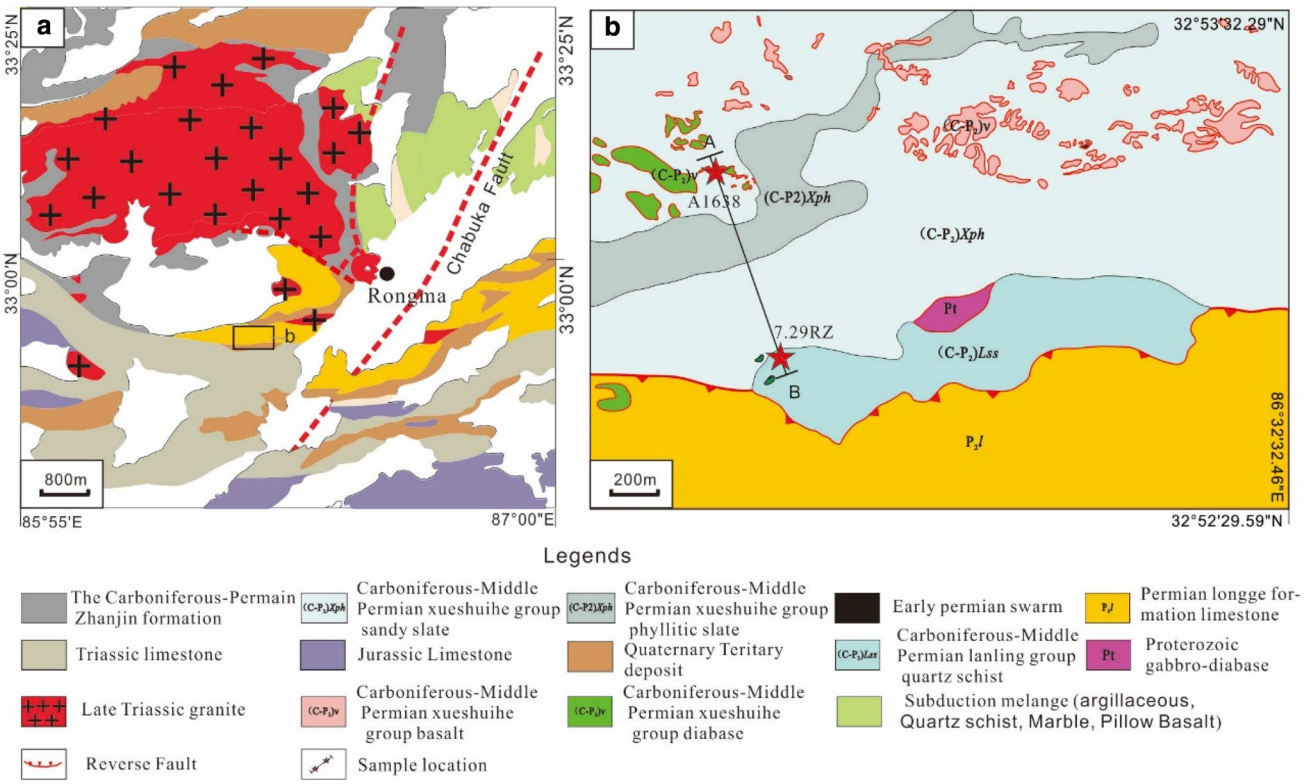

Fig. 2 a Simplified geological map of Rongma in the northern margin of the Southern Qiangtang block, northern Tibet (modified after Liu et al. 2011); **b** geological sketch map of Yadan area in the Rongma Town, in the northern margin of south Qiangtang

comprise the Paleozoic basalt fragments and the Cenozoic Nadingcuo Formation basalts. Regional metamorphic rocks mainly include garnet–phengite–quartz schist, blue schist, slab, phyllite, ampholite, marble, and metamorphic quartz sandstone (Fig. 2a, b). Field sections show that the garnet–phengite–quartz schist spreads nearly NW–SE, and is in fault contact with mafic rocks and marble (Fig. 3a). In addition, pillow basalt unconformable contact with garnet–phengite–quartz schist is also recognized in the area (Fig. 3b, c). Two stages of tectonic deformation can be observed in the region, with moderate–shallow layered shearing in the early stage, and secondary intense deformation due to N–S trending overthrusting in the late stage (Wang et al. 2019).

Petrography and methodology

Petrography

Diabase and garnet–phengite–quartz schist and gabbro samples were collected in Rongma Town, northern margin of southern Qiangtang, Tibet (Fig. 2b). Diabase (A1638) is colored off-grayish green, massive, with a fine diabasic

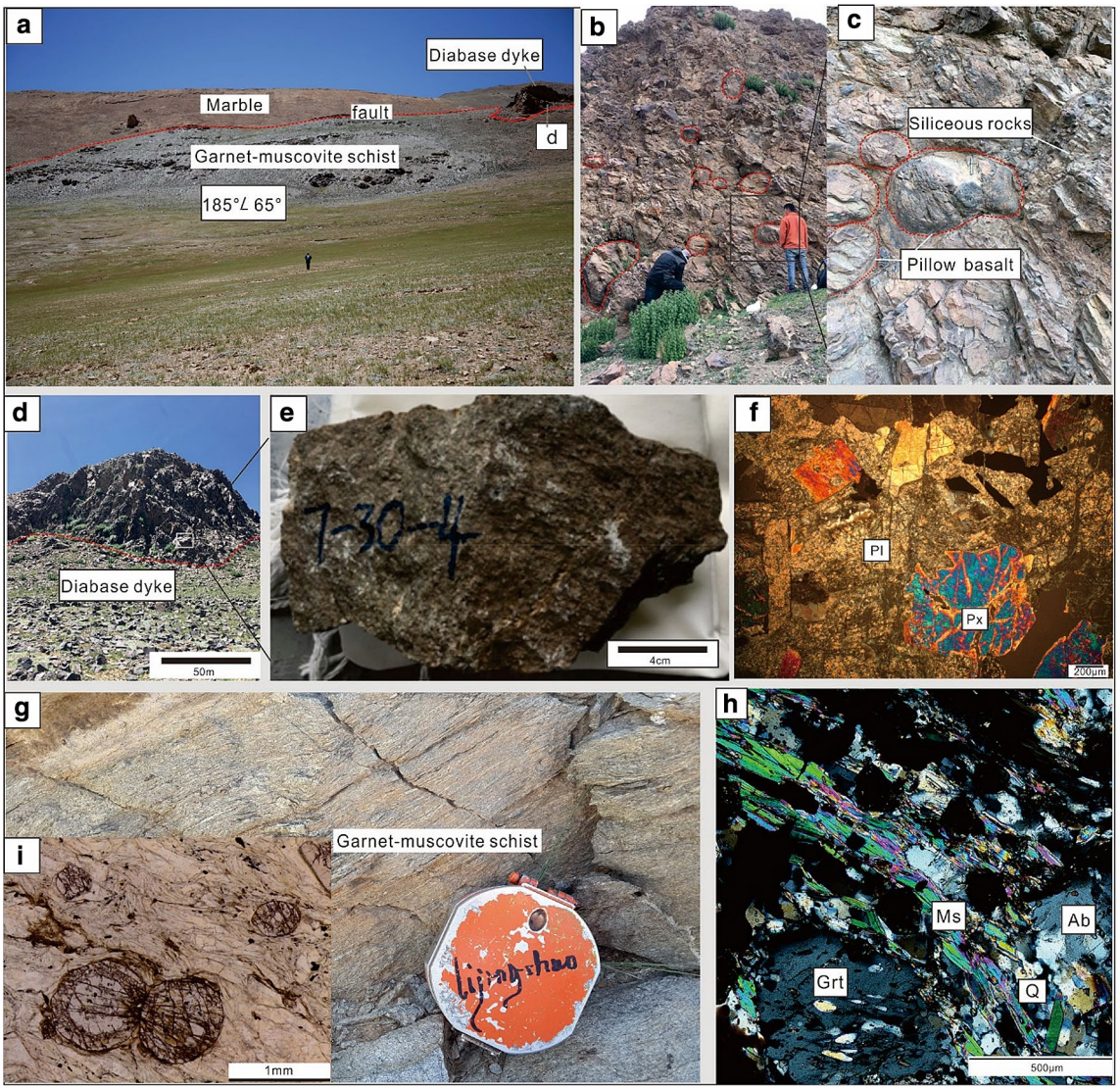

Fig. 3 Samples and microscopic characteristics of diabase and garnet–phengite–quartz schist from the Rongma area in the northern margin of south Qiangtang. **a** Field photo of garnet–phengite–quartz schist in fault contact with mafic rocks and marble; **b**, **c** pillow basalt and siliceous rocks; **d** field photo of the Early Triassic diabase dyke; **e** the Early Triassic diabase hand specimen; **f** Microscope photo of the diabase under cross-polarized light; **g** field photo of garnet–phengite–quartz schist; **h** microscope photo of garnet–phengite–quartz schist under cross-polarized light; **i** microscope photo of garnet in the garnet–phengite–quartz schist under single-polarized light. *Ab* albite, *Ms* phengite, *Pl* plagioclase, *Px* pyroxene, *Q* quartz, *Grt* garnet

texture. It mainly includes plagioclase (~55 vol.%) and secondary pyroxene (~40 vol.%) with minor minerals, such as apatite and magnetite. Plagioclase occurs as automorphic and hypautomorphic plates; plate lengths range from 0.2 to 1.5 mm. Plate crystals show intense sericitization and argillization, making the crystals muddy. Some of the crystals are wrapped by pyroxene, forming an ophitic texture. Pyroxene (Px) occurs as automorphic and hypautomorphic columns and grains, with minor octangular sections; grain sizes range from 0.2 to 2.2 mm. Some crystals wrap plagioclase, forming an ophitic texture. Minor crystals show serpentinization, with pseudomorphs of columnar crystals of primary minerals preserved. Also, minor nontransparent minerals are sporadically distributed and were allotriomorphic granular, with grain sizes of 0.1–1 mm (Fig. 3d–f). The Mayigangri gabbro (PM20) colored off-grayish green with a massive structure and a coarse grained texture. It mainly composed of plagioclase (~50 vol.%), clinopyroxene (~44 vol.%), amphibole, and biotite pseudoimage (~5 vol.%). The minor minerals include magnetite, chlorite, and epidote. Plagioclase is in the shape of hypidiomorphic plate or strip, which is distributed in the form of frame. Some plagioclases have been completely metasomatized and appear as pseudomorphs. Clinopyroxenes are subhedral columnar granular, filled between plagioclase crystals, and amphibole reaction edges can be seen locally (Gao et al. 2019).

Garnet–phengite–quartz schist shows a lepidogranoblastic texture and flaky structure, and it mainly comprises quartz (45 vol.%), phengite (35 vol.%), albite (10 vol.%), chlorite (5 vol.%), and garnet (5 vol.%). Structural fissures widely occurred and were filled with silicified quartz, minor sericite, and fragmented primary rocks as veins (Fig. 3g, h). In addition, overgrowth of garnet is common in garnet–phengite–quartz schist (Fig. 3i).

Methodology

In this study, one diabase sample was collected for U–Pb zircon dating and in-situ Hf isotope analyses, one garnet–phengite–quartz schist sample for U–Pb zircon dating, two groups of phengite samples of the schist for Ar–Ar dating, seven diabases and ten gabbros samples for whole-rock geochemical analysis, and four diabase samples for whole-rock Nd isotope analyses. Separation and selection of individual zircon grains were completed at the Laboratory of Beijing Zircon Chronology Navigator Technology Co., Ltd. Selected zircon grains and standard samples were imaged by transmission light, reflected light, and cathode luminescence microphotography for determination of zircon structure and genesis type. Appropriate testing positions away from cracks and inclusions were selected to avoid affecting data analysis quality. LA-ICP-MS U–Pb dating of zircon was performed using Thermo Element II at the Test Center of the Institute of Geology, Chinese Academy of Geological Science, using the instrument of the Finnigan Neptune-type MC-ICP-MS, and supporting Newwave UP 213 laser ablation system. Analytical spot sizes ~ 25 μm, with the frequency of 10 Hz, and the density of primary ion ~ 2.5 J/cm^2. Zircon GJ1 (U, 923 ppm; Th, 439 ppm; and Th/U, 0.475) is used as the external standards in zircon U–Pb dating calibration. The zircon Plešovice and standard samples GJ1 were tested twice, respectively, and once for every 10 spots to ensure the stability of the instrument. The method proposed by Andersen (2002) was adopted for common Pb correction and the international standard program Isoplot (ver3.0) was employed for age calculation. For analytical points with ages obtained as < 1 Ga, $^{206}Pb/^{238}U$ and the correspondent 1σ were used as the age, and $^{207}Pb/^{235}U$ and $^{206}Pb/^{238}U$ ratios were used to calculate the concordant degree; for analytical points with ages obtained as > 10 Ga, $^{207}Pb/^{206}Pb$ and the correspondent 1σ were used as the age, and the ratios of $^{207}Pb/^{206}Pb$ and $^{206}Pb/^{238}U$ were used to calculate the concordant degree. In the concordant degree calculation, 0.93–1.0 were adopted as the concordant points.

$^{40}Ar/^{39}Ar$ dating of phengite was performed at the Laboratory of Isotope Thermochronology, Institute of Geology, Chinese Academy of Geological Sciences. Sample heating by stage was completed using an electro-bombardment furnace. Mass spectrometry (MS) was conducted using a MM-1200B mass spectrometer. Quality discrimination correction, ammonia correction, blank correction, and interference element isotope correction were performed on all of the data. The sorted minerals (purity > 99%) were wrapped in aluminum foil, and placed in quartz vials and irradiated in the H4 position of the nuclear reactor at the China Institute of Atomic Energy, after being cleaned by ultrasonic waves. The standard biotite sample 2BH-25 is irradiated with integrated. The neutron flux was 2.60×10^{13} n cm^{-2} S^{-1} with the total irradiation time of 1440 min and an integrated neutron flux of 2.25×1018 n cm^{-2}. The irradiated samples were step heated in a graphite furnace. Each sample was heated for 10 min. Before being analyzed in a Helix MC noble gas mass spectrometer, the released gas was purified for 30 min. 20 cycles were measured at each peak. They were corrected by mass discrimination, atmospheric Ar contamination, interfering nuclear reactions, and procedural blanks, after all the data returned to zero-time values. The coefficients of interfered nuclear reactions generated by K and Ca during the neutron irradiation process were obtained from irradiated K_2SO_4 and CaF_2 samples with $(^{36}Ar/^{37}Aro)_{Ca} = 0.0002389$, and $(^{39}Ar/^{37}Aro)_{Ca} = 0.000806$, and $(^{40}Ar/^{39}Ar)_K = 0.004782$. The ^{40} K decay constant (λ) used was 5.543×10^{-10} year^{-1}, and ^{37}Ar was corrected for radioactive decay. The plateau age, isochronous age, and inverse isochronous age were calculated by the ISOPLOT program (Ludwig 2003).

Whole-rock major, trace, and rare-earth element analyses were completed at the Lab Center of Hebei CREC Geophysical Exploration Co., Ltd., and major elements were analyzed with an ARL Advant XP + XRF instrument, with a precision of more than 3%. Trace elements were analyzed using X-series 2/SN01831C ICP-MS, with a precision of more than 3%. Analytical procedures were similar to those described by Liu et al. (2016). In the digestion of samples, 0.5 g sample was mixed with 3 mL HF, 9 mL HNO_3, and 2 mL concentrated HCl at 108℃ for 24 h. The solution was evaporated to dryness and then was re-dissolved using 50 mL 2% (v/v) purified HNO_3 for analysis. The reference materials, including GSS1, GSS2, GSS3, and GSS4a from the Center of National Standard Reference Material of China, were chosen to check the precision of the analytical methods.

Diabase Nd isotope analyses were performed at the Lab Center of Nanjing University. Isotope testing was conducted by MC-ICPMS in a static mode at the Lab. USGS standard materials BHVO-2, BCR-2, and AGV-2 were employed in the entire analytical process for quality monitoring. $^{146}Nd/^{144}Nd = 0.7219$ was adopted for the internal correction of the equipment test according to index laws. Zircon in-situ Hf isotope analysis was performed by Laser Ablation MC-ICPMS at the Lab of Tianjin Geological Survey Center. The instrument system consisted of ESI NEW WAVE 193 nm FX laser and ThermoFisher NEPTUNE MC-ICPMS produced in the U.S.A. Performance parameters included a mass number range of 4–310 amu, resolution > 450 (flat peak, 10% peak valley definition), and abundance sensitivities < 5 ppm (without RPQ) and < 0.5 ppm (with RPQ). Measured peak stability included magnetic field and electric field drift (< 50 ppm/h), a laser pulse frequency of 8 Hz, and an ablation pore size 45 μm. Zircon GJ-1 was used as the standard for isotope monitoring, and zircon 91,500 as the correction standard.

Analytical results

Zircon U–Pb chronology

Zircon U–Pb dating is conducted on diabase and a garnet–phengite–quartz schist samples. A CL photo shows zircons from diabase occurred as plates and short columns, without oscillatory zonation (Fig. 4a, b); zircons from garnet–phengite–quartz schist have a complex shape, mainly ellipses and long and short columns. Some overgrowth zircons occurred in the schist samples and zircon punctuations are concentrated in the margins, but avoiding the accreting

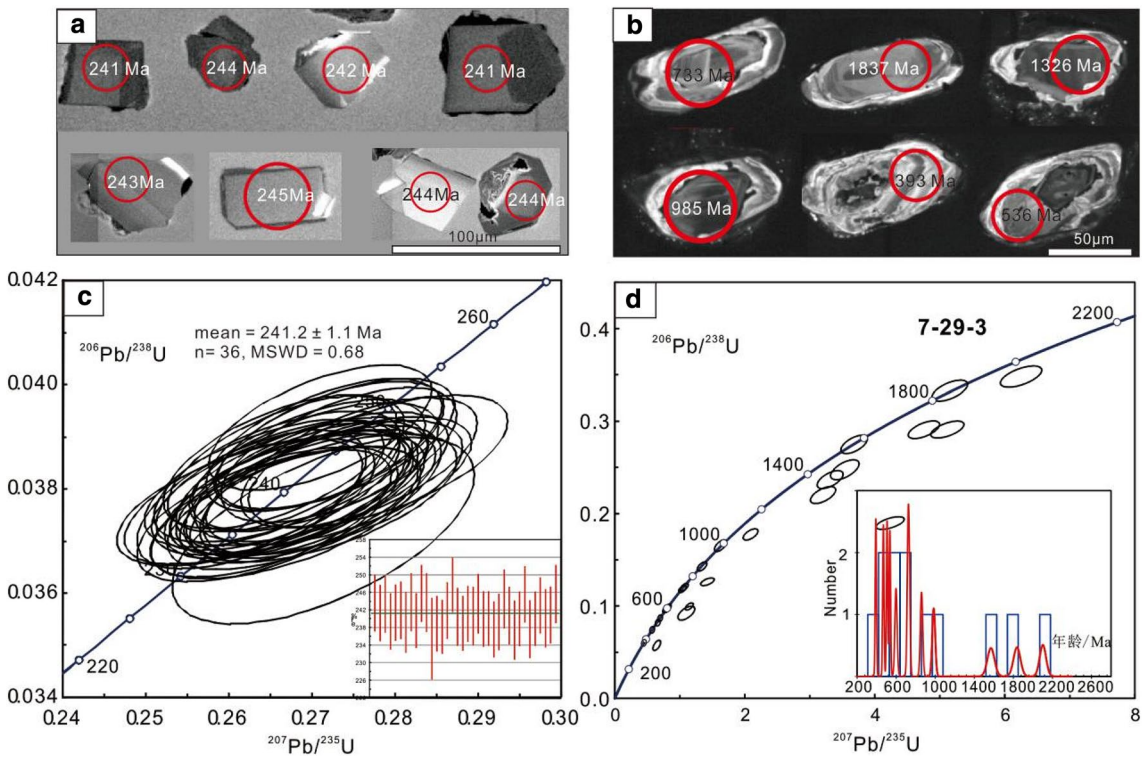

Fig. 4 Representative cathodoluminescence (CL) images of zircons from diabase sample A1638 in the northern margin of south Qiangtang. **a** Phengite–quartz schist sample 7.29RZ, and **b** U–Pb concordia diagrams of zircon data from samples A1638 (**c**) and 7.29RZ (**d**) from the Rongma area, Central Qiangtang

rims. Results of the analysis are shown in Table 1, and a zircon U–Pb concordia age diagram is shown in Fig. 4c, d.

The diabase (A16138) has zircon Th/U ratios between 0.6 and 3.7, indicating magmatic origin. Concordia ages of 36 zircon grains were obtained, and the weighted mean age was 241.2 ± 1.1 Ma (n = 36, MSWD = 0.68), representing the formation age of the diabase and indicating that it was formed in the Early Triassic Time (Table 1, Fig. 4c).

Zircons from the garnet–phengite–quartz schist (7.29RZ) display a complex configuration and roundness, reflecting complex zircon sources. Zircon Th/U ratios varied greatly, mainly from 0.04 to 0.98. The 16 analyses of zircons have a concordant degree of > 92% and seven were < 90%. The concordant ages are concentrated between 393 and 2102 Ma, indicating the protolith of this sample deposited after 393 Ma. The sample also have Precambrian zircon age data, including ~ 700 Ma, ~ 1000 Ma, ~ 1400 Ma, ~ 1800 Ma, and 2100 Ma (Table 1, Fig. 4d).

Phengite $^{40}Ar/^{39}Ar$ chronology

$^{40}Ar/^{39}Ar$ dating is conducted on two groups of phengite from the garnet–phengite–quartz schist. Stage heating dating analytical results of the phengite are shown in Table 2 and Fig. 5. Isochron diagrams of the two groups are shown in Fig. 5a, c, in which 12 stages of 790–1200 ℃ and 700–1400 ℃ constituted good age plateaus. tp_1 = 229.0 ± 1.4 Ma and tp_2 = 225.3 ± 1.3 Ma (Fig. 5b, d) correspond to ^{39}Ar release amounts of 98.4% and 99.65%, respectively. The corresponding $^{36}Ar/^{40}Ar$-$^{39}Ar/^{40}Ar$ isochron ages are t_{i1} = 227.7 ± 3.8 Ma and t_{i1} = 225.2 ± 2.1 Ma. Initialization values of $^{40}Ar/^{36}Ar$ were 305 ± 16 (MSWD = 36) and 296.0 ± 2.6 (MSWD = 4.6), respectively. Thus, ~ 229 to ~ 225 Ma could represent the formation time of the phengite, and reflect one stage of regional metamorphism event.

Major/trace/rare-earth elements

Elemental geochemical analyses are conducted on the Early Triassic diabase and gabbro samples in the Rongma area, and the data are shown in Table 3. The gabbro formed in the Early Triassic (~ 237 Ma, Gao et al. 2019). Seven diabase samples have SiO_2 of 47.82–49.60 wt.%, Al_2O_3 of 13.42–14.64 wt.%, TiO_2 of 1.55–1.94 wt.%, MgO of 8.10–8.76 wt.%, MgO/FeOt of 1.23–1.42, and LOI of 3.10–6.27 wt.%. Ten gabbro samples show SiO_2 of 46.12–48.38 wt.%, Al_2O_3 of 10.24–15.14 wt.%, TiO_2 of 1.31–2.47 wt.%, MgO of 4.52–12.60 wt.%, MgO/FeOt of 0.50–1.70, and LOI of 3.09 ~ 8.35 wt.%. Given the relatively high LOI, some relatively stable elements, e.g., high field-strength elements (HFSEs) were used to determine petrogenesis. On the whole-rock SiO_2-Nb/Y and Zr/TiO_2-Nb/Y diagrams (Winchester and Floyd 1977; Zhou et al. 2009), all the diabase and most gabbro samples fall in the sub-alkaline basalt field (Fig. 6a, b). On the trace element and rare-earth element (REE)-normalized diagrams (Fig. 7a, b), the seven diabase and ten gabbro samples overall showed geochemical features similar to continental arc basalt despite with high LOI values (Table 3). Diabase samples mainly show weak negative Nb, Ta, and Th anomalies and positive Pb anomaly with total rare-earth elements concentrations (ΣREEs) of 79–89 ppm and chondrite-normalized REE patterns imply they have a typical right-inclined tendency with $(La/Yb)_N$ = 5.65–6.14 and with weak positive Eu anomalies (δEu = 1.02–1.20) (Table 3, Fig. 7a, b). However, gabbros are weak depletion in Nb, Ta, and Th, enrichment in Pb, and have variable ΣREEs of 56–119 ppm. They have a typical right-inclined tendency with $(La/Yb)_N$ = 4.74–5.65 and with weak negative to weak positive Eu anomalies (δEu = 0.76–1.12) in chondrite-normalized REE patterns (Table 3, Fig. 7a, b). In addition, both diabases and gabbros mainly display signatures of a calc-alkali-potassium basaltic series (Fig. 8a, b).

Whole-rock Nd and Hf-in-zircon isotopes

Whole-rock Nd and zircon Hf isotopes analyses are conducted on the Early Triassic diabase. Analytical results are shown in Tables 4 and 5. The rock have a $^{143}Nd/^{144}Nd$ ratio between 0.512504 and 0.512514, and $\varepsilon_{Nd}(t)$ of − 0.8 ~ 0.9. Zircon $^{176}Hf/^{177}Hf$ ratio ranges widely from 0.282629 to 0.283184, with ε_{Hf} (t) of − 0.6 ~ 19.1, and T_{DM} of 498 ~ 991 M (removed two bad data $t > T_{DM}$ of 105 Ma and 131 Ma) (Tables 4, 5; Fig. 9a, b).

Mineral chemistry and thermobarometric evaluation

Based on petrographic observations for the garnet–phengite–quartz schist from Rongma area, three stages of mineral assemblages have been recognized. Peak metamorphic stage mineral assemblages are garnet + phengite + quartz. The early retrograde metamorphic mineral assemblages are composed of garnet, phengite, biotite, chlorite and quartz, and the late retrograde metamorphic mineral assemblages consist of garnet, phengite, biotite, chlorite, albite, and quartz. On the basis of detailed petrographic and mineralogical observation, representative samples were selected for further phase equilibrium model (Fig. 10). It mainly include garnet, phengite, quartz, albite and minor sphene, rutile, albite, and chlorite. The phase equilibrium model was performed using Domino/theriak software (de Capitani and Petrakakis 2010) through the following mineral solid solution models: epidote (Holland and Powell 1998), plagioclase (Baldwin et al. 2005; Holland and Powell 2003), garnet (White et al. 2005), omphacite (Green et al. 2007), chlorite

Table 1 U–Pb isotope compositions of the zircons from diabase and garnet–phengite–quartz schist from Rongma town in the northern margin of south Qiangtang

Analysis no	Content(ppm)			Th/U	Isotopic ratio						Age (Ma)						Degree of harmonic
	Pb	Th	U		$^{206}Pb/^{238}U$	1σ	$^{207}Pb/^{235}U$	1σ	$^{207}Pb/^{206}Pb$	1σ	$^{206}Pb/^{238}U$	1σ	$^{207}Pb/^{235}U$	1σ	$^{207}Pb/^{206}Pb$	1σ	
Diabase																	
A16138.2.1	81	2615	1433	1.8	0.0385	0.0005	0.2757	0.0058	0.0519	0.0010	244	3	247	5	282	45	0.99
A16138.2.2	44	1481	794	1.9	0.0381	0.0005	0.2687	0.0062	0.0511	0.0011	241	3	242	6	245	50	1.00
A16138.2.3	162	7864	2132	3.7	0.0385	0.0005	0.2696	0.0057	0.0508	0.0010	243	3	242	5	232	45	1.00
A16138.2.4	32	932	630	1.5	0.0378	0.0005	0.2713	0.0066	0.0520	0.0012	239	3	244	6	286	53	0.98
A16138.2.5	50	1842	851	2.2	0.0382	0.0005	0.2732	0.0065	0.0519	0.0012	241	3	245	6	282	52	0.98
A16138.2.6	89	3463	1487	2.3	0.0382	0.0005	0.2658	0.0061	0.0504	0.0010	242	3	239	5	214	47	0.99
A16138.2.7	242	7714	4634	1.7	0.0378	0.0005	0.2627	0.0056	0.0504	0.0010	239	3	237	5	214	44	0.99
A16138.2.8	35	946	710	1.3	0.0385	0.0005	0.2779	0.0064	0.0523	0.0011	244	3	249	6	299	49	0.98
A16138.2.9	44	1380	843	1.6	0.0379	0.0005	0.2672	0.0061	0.0512	0.0011	240	3	240	6	249	49	1.00
A16138.2.10	160	6299	2189	2.9	0.0414	0.0006	0.2911	0.0063	0.0510	0.0010	261	4	259	6	242	45	0.99
A16138.2.11	93	2776	1653	1.7	0.0405	0.0006	0.2811	0.0063	0.0503	0.0010	256	4	252	6	210	46	0.98
A16138.2.12	158	6090	2557	2.4	0.0389	0.0005	0.2728	0.0059	0.0509	0.0010	246	3	245	5	236	46	1.00
A16138.2.13	125	4549	2147	2.1	0.0385	0.0005	0.2661	0.0057	0.0501	0.0010	244	3	240	5	200	46	0.98
A16138.2.14	80	1195	1959	0.6	0.0372	0.0007	0.2713	0.0074	0.0529	0.0011	235	5	244	7	324	48	0.96
A16138.2.15	28	762	573	1.3	0.0378	0.0005	0.2620	0.0063	0.0503	0.0012	239	3	236	6	211	53	0.99
A16138.2.16	52	1612	973	1.7	0.0376	0.0005	0.2677	0.0062	0.0516	0.0011	238	3	241	6	267	50	0.99
A16138.2.17	64	2050	1178	1.7	0.0382	0.0005	0.2711	0.0062	0.0514	0.0011	242	3	244	6	260	49	0.99
A16138.2.18	232	9425	3434	2.7	0.0392	0.0005	0.2710	0.0055	0.0502	0.0009	248	3	243	5	202	43	0.98
A16138.2.19	34	1012	653	1.5	0.0380	0.0005	0.2664	0.0064	0.0508	0.0012	240	3	240	6	233	53	1.00
A16138.2.20	72	2229	1347	1.7	0.0378	0.0005	0.2617	0.0058	0.0503	0.0010	239	3	236	5	207	48	0.99
A16138.2.21	111	4322	1762	2.5	0.0381	0.0005	0.2642	0.0059	0.0503	0.0010	241	3	238	5	208	48	0.99
A16138.2.22	70	2027	1329	1.5	0.0380	0.0005	0.2724	0.0064	0.0520	0.0011	241	3	245	6	283	49	0.98
A16138.2.23	95	3209	1594	2.0	0.0385	0.0005	0.2668	0.0058	0.0503	0.0010	243	3	240	5	208	47	0.99
A16138.2.24	74	2458	1305	1.9	0.0379	0.0005	0.2697	0.0062	0.0516	0.0011	240	3	242	6	267	49	0.99
A16138.2.25	61	1957	1145	1.7	0.0379	0.0005	0.2678	0.0061	0.0512	0.0011	240	3	241	5	249	50	1.00
A16138.2.26	175	4550	3161	1.4	0.0418	0.0006	0.2964	0.0063	0.0514	0.0010	264	4	264	6	260	43	1.00
A16138.2.27	58	1726	1144	1.5	0.0375	0.0005	0.2650	0.0059	0.0512	0.0011	238	3	239	5	250	49	1.00
A16138.2.28	63	1951	1215	1.6	0.0378	0.0005	0.2688	0.0060	0.0515	0.0011	239	3	242	5	265	47	0.99
A16138.2.29	131	4610	2255	2.0	0.0387	0.0005	0.2732	0.0058	0.0513	0.0010	244	3	245	5	252	45	1.00
A16138.2.30	103	3557	1844	1.9	0.0380	0.0005	0.2693	0.0060	0.0513	0.0010	241	3	242	5	256	47	0.99
A16138.2.31	57	2256	979	2.3	0.0375	0.0005	0.2646	0.0064	0.0511	0.0012	237	3	238	6	248	52	1.00
A16138.2.32	86	2814	1612	1.7	0.0379	0.0005	0.2675	0.0057	0.0511	0.0010	240	3	241	5	247	46	1.00
A16138.2.33	135	4251	2465	1.7	0.0388	0.0005	0.2720	0.0056	0.0508	0.0010	246	3	244	5	232	44	0.99
A16138.2.34	37	1143	728	1.6	0.0376	0.0005	0.2668	0.0066	0.0515	0.0012	238	3	240	6	265	53	0.99
A16138.2.35	67	2293	1237	1.9	0.0379	0.0005	0.2674	0.0059	0.0511	0.0010	240	3	241	5	246	47	1.00

Table 1 (continued)

Analysis no	Content(ppm)			Th/U	Isotopic ratio						Age (Ma)						Degree of harmonic
	Pb	Th	U		$^{206}Pb/^{238}U$	1σ	$^{207}Pb/^{235}U$	1σ	$^{207}Pb/^{206}Pb$	1σ	$^{206}Pb/^{238}U$	1σ	$^{207}Pb/^{235}U$	1σ	$^{207}Pb/^{206}Pb$	1σ	
A16138.2.36	59	1964	1076	1.8	0.0384	0.0005	0.2702	0.0061	0.0510	0.0011	243	3	243	6	241	49	1.00
A16138.2.37	282	11,610	4387	2.6	0.0380	0.0005	0.2710	0.0059	0.0518	0.0010	240	3	243	5	276	46	0.99
A16138.2.38	61	1817	1204	1.5	0.0381	0.0005	0.2658	0.0060	0.0506	0.0011	241	3	239	5	225	48	0.99
A16138.2.39	231	8978	3698	2.4	0.0388	0.0005	0.2714	0.0058	0.0507	0.0010	246	3	244	5	226	45	0.99
Polysilicon-muscovite-quartz schist																	
7.29.RZ1.1	209	283	690	0.4	0.2907	0.0039	4.7567	0.0986	0.1187	0.0022	1645	22	1777	37	1936	34	0.92
7.29.RZ1.3	29	137	212	0.6	0.1204	0.0017	1.0713	0.0243	0.0645	0.0014	733	10	739	17	759	45	0.99
7.29.RZ1.5	45	176	505	0.3	0.0819	0.0011	0.6625	0.0193	0.0587	0.0016	507	7	516	15	555	59	0.98
7.29.RZ1.6	15	57	140	0.4	0.0974	0.0019	0.8040	0.0263	0.0599	0.0015	599	12	599	20	600	55	1.00
7.29.RZ1.8	127	223	486	0.5	0.2368	0.0040	3.3133	0.0813	0.1015	0.0020	1370	23	1484	36	1652	36	0.92
7.29.RZ1.9	60	95	162	0.6	0.3328	0.0046	5.1549	0.1118	0.1123	0.0022	1852	26	1845	40	1837	35	1.00
7.29.RZ1.10	289	316	757	0.4	0.3479	0.0047	6.2515	0.1300	0.1303	0.0024	1925	26	2012	42	2102	33	0.95
7.29.RZ1.11	56	193	272	0.7	0.1774	0.0025	2.0899	0.0465	0.0854	0.0018	1053	15	1145	25	1326	40	0.91
7.29.RZ1.13	59	413	423	1.0	0.1184	0.0016	1.0412	0.0237	0.0638	0.0013	721	10	724	17	735	42	1.00
7.29.RZ1.14	40	47	283	0.2	0.1428	0.0020	1.3432	0.0300	0.0682	0.0014	860	12	865	19	875	42	1.00
7.29.RZ1.15	142	120	563	0.2	0.2474	0.0044	3.5402	0.0894	0.1038	0.0020	1425	25	1536	39	1693	35	0.92
7.29.RZ1.17	76	138	252	0.5	0.2748	0.0041	3.6827	0.0833	0.0972	0.0019	1565	23	1568	35	1571	36	1.00
7.29.RZ1.18	19	2	319	0.0	0.0628	0.0010	0.4842	0.0146	0.0559	0.0015	393	7	401	12	449	59	0.98
7.29.RZ1.19	29	25	349	0.1	0.0867	0.0011	0.6984	0.0158	0.0584	0.0012	536	7	538	12	545	46	1.00
7.29.RZ1.21	44	148	248	0.6	0.1652	0.0025	1.6254	0.0371	0.0714	0.0014	985	15	980	22	968	40	0.99
7.29.RZ1.23	29	51	386	0.1	0.0755	0.0011	0.5918	0.0169	0.0568	0.0016	469	7	472	13	486	61	0.99

Table 2 Result of $^{39}Ar/^{40}Ar$ stepwise heating dating for phengite of garnet–phengite–quartz schist from Rongma area in the northern margin of south Qiangtang

T(°C)	$(^{40}Ar/^{39}Ar)_m$	$(^{36}Ar/^{39}Ar)_m$	$(^{37}Ar_0/^{39}Ar)_m$	$(^{38}Ar/^{39}Ar)_m$	^{40}Ar (%)	F	$^{39}Ar(\times 10^{-14}$ mol)	^{39}Ar(Cum.) (%)	Age (Ma)	$\pm 1\sigma$ (Ma)
7-19-DF3										
700	108.9195	0.2245	0.0457	0.0579	39.09	42.5747	0.04	0.35	156	9.4
770	71.9031	0.0338	0.4295	0.0216	86.13	61.9523	0.44	4.08	222.8	2.3
820	68.2905	0.0171	0.0656	0.0156	92.58	63.2269	0.71	10.08	227.1	2.2
850	66.6172	0.0119	0.0000	0.0144	94.7	63.0876	0.68	15.83	226.7	2.2
890	65.5181	0.0095	0.0000	0.0142	95.72	62.7147	1.65	29.81	225.4	2.1
920	64.4599	0.0062	0.0106	0.0141	97.14	62.6162	1.81	45.15	225.1	2.1
950	65.2266	0.0085	0.0000	0.014	96.16	62.7228	1.28	55.97	225.4	2.1
980	65.5374	0.0103	0.0666	0.0151	95.34	62.4896	1.27	66.7	224.6	2.1
1020	64.9027	0.0076	0.0000	0.0143	96.53	62.652	1.98	83.47	225.2	2.1
1060	76.1447	0.0462	0.0245	0.0217	82.08	62.4996	1.2	93.64	224.7	2.1
1120	80.4407	0.0601	0.1016	0.0236	77.94	62.7008	0.42	97.24	225.3	2.3
1200	196.3103	0.4514	0.0692	0.0984	32.06	62.9385	0.33	100	226.1	2.3
8-15-4DF1										
700	150.5493	0.3716	1.4613	0.0916	27.13	40.8916	0.08	0.63	157.9	4.8
770	92.7921	0.1067	0.0312	0.0338	66.02	61.2648	0.84	7.48	231.7	2.2
800	89.8411	0.0975	0.0000	0.0315	67.94	61.036	0.73	13.47	230.9	2.2
840	82.2781	0.0726	0.0000	0.0259	73.91	60.8136	1.29	24.05	230.1	2.2
870	75.0466	0.0496	0.0099	0.0221	80.47	60.3887	1.26	34.35	228.6	2.2
900	70.3756	0.0344	0.0407	0.0193	85.54	60.2013	1.4	45.87	227.9	2.2
940	70.0611	0.0338	0.0385	0.019	85.74	60.0735	1.63	59.25	227.5	2.2
980	71.7081	0.0372	0.0802	0.0202	84.69	60.7305	1.52	71.76	229.8	2.2
1020	67.5125	0.0201	0.0176	0.0164	91.2	61.5705	1.8	86.15	232.8	2.2
1060	65.3511	0.0195	0.1400	0.0168	91.21	59.6106	0.86	93.6	225.8	2.2
1140	62.563	0.0107	0.0000	0.0148	94.93	59.3932	0.66	99	225	2.3
1400	120.892	0.2067	0.5186	0.0546	49.51	59.8573	0.12	100	226.8	2.8

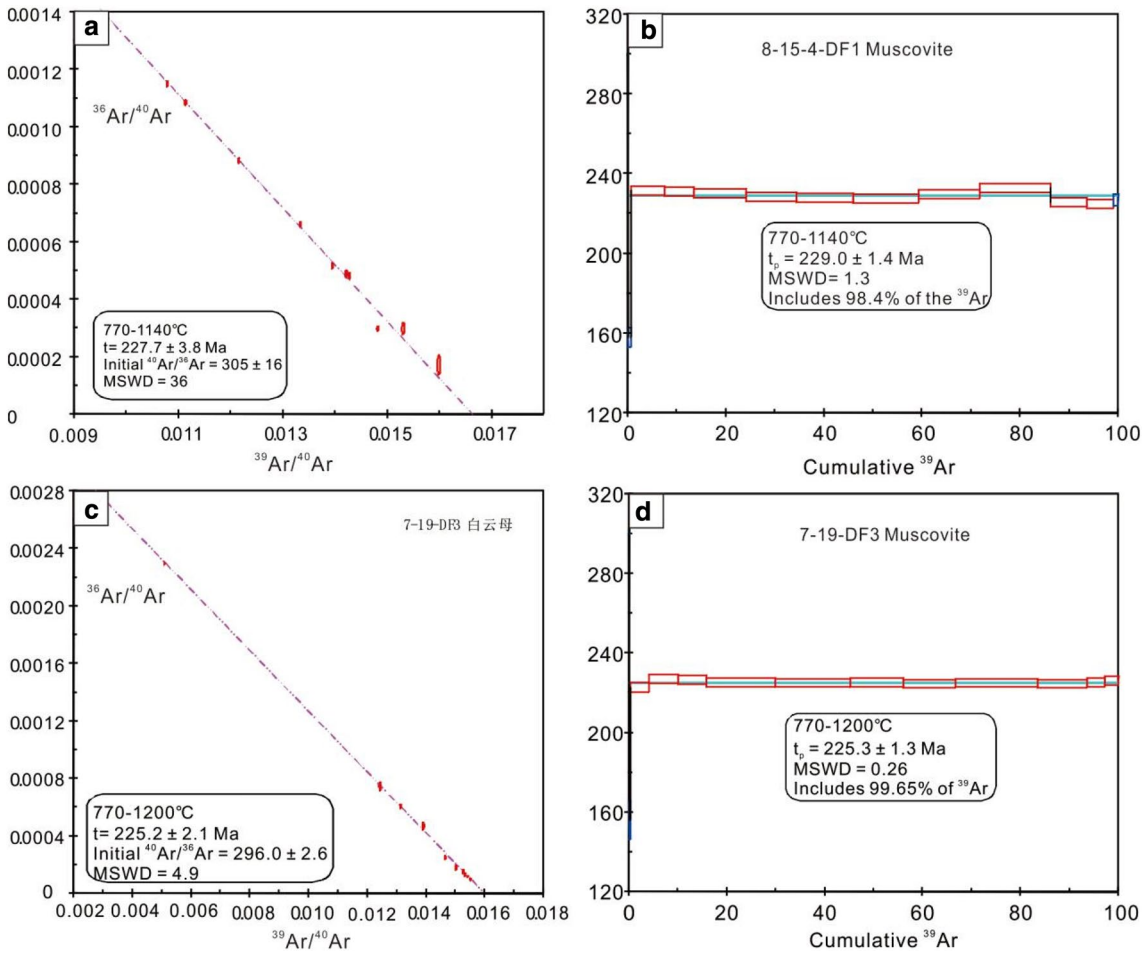

Fig. 5 **a**, **c** Isochronic age, and **b**, **d** $^{40}Ar/^{39}Ar$ plateau age diagrams of phengite from the garnet–phengite–quartz schist from the Rongma area in the northern margin of south Qiangtang

(Holland and Powell 1998), muscovite (Coggon and Holland 2002), biotite (White et al. 2007), talc (Holland and Powell 1998), chlorite (White et al. 2000), magnetite (White et al. 2007), and hornblende (Diener et al. 2007). Other minerals, such as quartz/coesite, kyanite, water, and andalusite, are end member minerals.

Since garnet in the sample has obviously experienced two stages of growth (Fig. 10a–d), and the core and overgrowth rim record distinct compositions of grossular, pyrope, spessartine, and almandine (Fig. 10d). The pressure and temperature conditions (P–T) of garnet core formation is simulated according to whole-rock geochemical data (Table 6). Electron probe data (Table 7) and the effective whole-rock composition obtained from mineral volume (Carson et al. 1999) were used to simulate phase equilibria for the P–T conditions of garnet overgrowth rim. Considering that TiO_2 and P_2O_5 only exist in accessory minerals and have little content in main silicate minerals, their influence on phase diagram is ignored. MnO is mainly concentrated in garnet core, which has great influence on garnet stability (Wei et al. 2004). Fe_2O_3 has great influence on the stability domain of amphibole (Du et al. 2014). Therefore, the model system of MnO-Na_2O-CaO-K_2O-FeOt-MgO-Al_2O_3-SiO_2-H_2O (MNCKFMASHO) is used to simulate the metamorphic process of rocks, and the excess of Q and H_2O is assumed.

Measured P–T profile (Fig. 11) is calculated by whole-rock composition of garnet phengite schist in MNCKF-MASHO system. The phase diagram shows that garnet is stable in most regions and only disappears at 350–460 ℃/14–21 kbar and 350–440 ℃/5–13 kbar. Biotite is stable in the range of 440–650 ℃/5–14 kbar. Lawsonite is stable in the range of 350–540 ℃/9–30 kbar. Epidote is stable in the range of 350–500 ℃/5–15 kbar. Chlorite is stable in the range of 350–520 ℃/5–17 kbar. The isopleth of grossular, pyrope, and spessartine contents in garnet are also calculated. In most regions, the grossular isopleth has relatively steep slopes, and grossular content decreases gradually with the increase of temperature. The content of pyrope increases gradually with the increase of temperature and their isopleth have variable slopes in

Table 3 Major elements (wt.%), trace elements (ppm), and REE (ppm) concentrations of the Early Triassic diabase and gabbro from Rongma area in the northern margin of south Qiangtang, and average trace elements (ppm) and REE (ppm) concentrations of OIB, E-MORB, N-MORB, and continental arc basalt (CAB)

Sample no	A1638-1	A1638-2	A1638-3	A1638-4	A1638-5	A1638-6	A1638-7	PM20-1	PM20-2	PM20-3	PM20-4	PM20-5	PM20-6	PM20-7	PM20-8	PM20-9	PM20-10	N-MORB	E-MORB	OIB	CAB
SiO_2	49.53	49.60	49.31	48.27	49.00	48.66	47.82	47.32	47.22	48.38	46.32	46.12	48.06	47.42	47.33	47.73	47.42	–	–	–	–
Al_2O_3	13.42	14.01	13.77	14.54	14.46	14.64	14.20	15.14	10.24	12.58	13.51	12.99	13.13	12.68	14.18	12.42	13.07	–	–	–	–
TFe_2O_3	8.65	8.61	8.75	7.55	7.36	7.56	7.49	2.61	2.06	3.45	2.21	2.25	1.81	2.53	2.92	3.75	3.20	–	–	–	–
MgO	8.70	8.76	8.47	8.41	8.16	8.33	8.10	7.86	12.60	4.52	6.12	6.95	6.52	10.39	9.24	8.67	9.42	–	–	–	–
CaO	10.30	9.72	9.44	9.19	9.45	8.91	9.87	10.74	11.74	9.23	8.39	8.19	6.44	14.06	13.40	11.69	12.14	–	–	–	–
Na_2O	3.28	2.55	2.61	3.83	3.85	3.66	3.76	2.21	1.32	2.82	2.41	2.75	2.75	1.32	1.70	1.84	1.65	–	–	–	–
K_2O	0.67	1.26	1.28	0.55	0.53	0.77	0.47	1.61	0.86	1.58	1.52	1.39	1.04	0.61	0.90	1.13	1.09	–	–	–	–
MnO	0.13	0.14	0.13	0.13	0.13	0.13	0.13	0.16	0.16	0.20	0.21	0.19	0.16	0.12	0.12	0.16	0.13	–	–	–	–
TiO_2	1.86	1.91	1.94	1.59	1.55	1.65	1.63	1.31	1.83	2.47	1.72	2.06	1.48	1.29	1.35	1.98	1.77	–	–	–	–
P_2O_5	0.15	0.16	0.16	0.14	0.10	0.10	0.10	0.16	0.16	0.22	0.24	0.17	0.21	0.10	0.12	0.16	0.14	–	–	–	–
LOI	3.14	3.10	3.93	5.65	5.26	5.41	6.27	4.03	3.59	4.89	8.35	7.96	9.11	3.13	3.09	3.07	3.40	–	–	–	–
FeO	6.67	6.88	6.88	6.13	5.73	5.97	5.99	6.83	7.96	9.08	8.72	8.60	8.60	6.10	5.44	7.15	6.34	–	–	–	–
Rb	34.93	46.41	53.19	25.42	30.34	42.91	30.75	61.10	26.90	33.50	37.70	33.50	22.40	22.50	25.50	40.90	34.30	0.56	5.04	31.00	18.63
Ba	474.14	661.10	786.54	387.07	346.90	501.68	353.26	433	269.80	867.40	477.10	635.50	504.50	193.90	230.10	292.20	397.40	6.30	57.00	350.00	295.04
Th	1.80	1.95	2.15	2.07	1.69	1.66	1.78	3.92	2.77	3.77	2.83	3.20	2.98	2.22	1.79	3.22	3.06	0.12	0.60	4.00	2.03
U	0.57	0.58	0.64	0.61	0.53	0.52	0.56	0.83	0.62	0.76	0.67	0.71	0.67	0.54	0.48	0.69	0.76	0.05	0.18	1.02	0.53
K	5753	10800	11116	4856	4641	6782	4201	13365	7139	13116	12618	11539	8633	5064	7471	9380	9048	600	2100	12000	7302
Ta	0.93	0.87	0.88	0.71	0.78	0.85	0.83	0.98	0.60	0.98	0.76	1.00	0.88	0.56	0.55	1.04	0.90	0.13	0.47	2.70	0.45
Nb	10.90	11.36	11.49	9.85	9.58	9.81	9.43	10.80	8.00	13.80	10.20	10.70	9.50	7.79	7.56	16.25	13.18	2.33	8.30	48.00	6.23
La	14.11	14.78	15.20	13.99	12.68	12.65	13.54	16.32	14.58	17.54	18.39	15.21	17.01	10.09	8.41	16.97	16.38	2.50	6.30	37.00	11.85
Ce	33.28	30.15	31.05	28.44	28.91	30.73	31.19	35.81	31.79	41.21	41.77	34.68	38.59	23.12	19.49	38.21	36.84	7.50	15.00	80.00	25.87
Pb	9.66	2.65	3.40	3.66	9.47	9.40	10.23	7.60	5.00	5.40	6.40	13.60	9.80	5.35	4.01	15.10	6.68	0.30	0.60	3.20	3.36
Pr	4.03	4.22	4.33	3.92	3.63	3.61	3.73	4.78	4.34	5.66	5.82	4.74	5.35	3.15	2.67	5.24	4.90	1.32	2.05	9.70	2.85
Sr	570	656	619	641	666	671	633	345	216	313	342	377	291	508	390	286	250	90	155	660	426
P	661	685	694	633	431	458	440	698	698	960	1048	742	917	436	528	703	629	510	620	2700	961
Nd	17.40	18.17	18.31	16.46	15.40	15.37	15.67	20.21	18.76	24.69	24.87	20.67	22.92	13.76	11.80	22.38	20.67	7.30	9.00	38.50	14.88
Zr	105.14	159.96	162.52	144.52	95.49	96.60	94.76	308.7	222.70	211.30	333.40	366.00	281.90	95.80	92.70	135.40	122.00	74.00	73.00	280.00	92.70
Hf	3.03	4.35	4.40	4.01	2.71	2.77	2.76	2.43	1.88	2.38	2.83	3.02	2.40	3.40	3.13	4.46	4.02	2.05	2.03	7.80	2.14
Sm	4.02	4.25	4.13	3.75	3.66	3.60	3.62	4.77	4.59	6.01	6.14	5.03	5.58	3.56	3.02	5.47	5.11	2.63	2.60	10.00	3.43
Eu	1.50	1.51	1.49	1.28	1.48	1.41	1.46	1.57	1.41	1.90	1.90	1.58	1.33	1.23	1.02	1.72	1.71	1.02	0.91	3.00	1.07
Ti	11527	11841	12155	10096	9820	10472	10469	7853	10971	14808	10311	12350	8873	7734	8093	11870	10611	7600	6000	17200	5880
Dy	3.94	4.04	4.04	3.66	3.54	3.55	3.52	4.68	4.40	5.74	5.79	4.91	5.34	3.54	2.90	5.25	4.79	4.55	3.55	5.6	3.32
Y	19.13	19.42	19.30	17.30	17.02	16.91	16.71	22.37	20.79	26.05	26.43	22.24	23.82	16.36	13.36	23.85	21.99	28	22	29	18.69
Ho	0.75	0.77	0.75	0.69	0.67	0.67	0.67	0.89	0.83	1.08	1.08	0.95	0.99	0.65	0.53	0.96	0.86	1.01	0.79	1.06	0.68
Yb	1.79	1.82	1.84	1.64	1.59	1.58	1.58	2.31	2.12	2.68	2.68	2.30	2.45	1.48	1.17	2.26	2.08	3.05	2.37	2.16	1.82
Lu	0.25	0.25	0.26	0.23	0.22	0.23	0.22	0.41	0.37	0.44	0.52	0.46	0.45	0.30	0.24	0.49	0.43	0.455	0.354	0.3	0.28
La	14.11	14.78	15.20	13.99	12.68	12.65	13.54	16.32	14.58	17.54	18.39	15.21	17.01	10.09	8.41	16.97	16.38	2.5	6.3	37	11.85
Ce	33.28	30.15	31.05	28.44	28.91	30.73	31.19	35.81	31.79	41.21	41.77	34.68	38.59	23.12	19.49	38.21	36.84	7.5	15	80	25.87
Pr	4.03	4.22	4.33	3.92	3.63	3.61	3.73	4.78	4.34	5.66	5.82	4.74	5.35	3.15	2.67	5.24	4.90	1.32	2.05	9.7	2.85

Table 3 (continued)

Sample no	A1638-1	A1638-2	A1638-3	A1638-4	A1638-5	A1638-6	A1638-7	PM20-1	PM20-2	PM20-3	PM20-4	PM20-5	PM20-6	PM20-7	PM20-8	PM20-9	PM20-10	N-MORB	E-MORB	OIB	CAB
Nd	17.40	18.17	18.31	16.46	15.40	15.37	15.67	20.21	18.76	24.69	24.87	20.67	22.92	13.76	11.80	22.38	20.67	7.3	9	38.5	14.88
Sm	4.02	4.25	4.13	3.75	3.66	3.60	3.62	4.77	4.59	6.01	6.14	5.03	5.58	3.56	3.02	5.47	5.11	2.63	2.6	10	3.43
Eu	1.50	1.51	1.49	1.28	1.48	1.41	1.45	1.57	1.41	1.90	1.90	1.58	1.33	1.23	1.02	1.72	1.71	1.02	0.91	3	1.07
Gd	4.26	4.33	4.35	3.92	3.83	3.96	3.87	4.54	4.27	5.50	5.51	4.64	5.14	3.17	2.65	4.88	4.48	3.68	2.97	7.62	3.55
Tb	0.71	0.74	0.73	0.67	0.65	0.65	0.64	0.81	0.77	1.00	1.00	0.85	0.94	0.64	0.52	0.94	0.87	0.67	0.53	1.05	0.51
Dy	3.94	4.04	4.04	3.66	3.54	3.55	3.52	4.68	4.40	5.74	5.79	4.91	5.34	3.54	2.90	5.25	4.79	4.55	3.55	5.6	3.32
Ho	0.75	0.77	0.75	0.69	0.67	0.67	0.67	0.89	0.83	1.08	1.08	0.95	0.99	0.65	0.53	0.96	0.86	1.01	0.79	1.06	0.68
Er	1.94	1.76	1.76	1.61	2.12	1.89	1.82	2.33	2.19	2.88	2.91	2.43	2.64	1.83	1.47	2.68	2.44	2.97	2.31	2.62	1.95
Tm	0.28	0.28	0.28	0.26	0.25	0.25	0.24	0.38	0.35	0.44	0.45	0.38	0.42	0.28	0.23	0.43	0.38	0.456	0.356	0.35	0.29
Yb	1.79	1.82	1.84	1.64	1.59	1.58	1.58	2.31	2.12	2.68	2.68	2.30	2.45	1.48	1.17	2.26	2.08	3.05	2.37	2.16	1.82
Lu	0.25	0.25	0.26	0.23	0.22	0.23	0.22	0.41	0.37	0.44	0.52	0.46	0.45	0.30	0.24	0.49	0.43	0.455	0.354	0.3	0.28
Y	19.13	19.42	19.30	17.30	17.02	16.91	16.71	22.37	20.79	26.05	26.43	22.24	23.82	16.36	13.36	23.85	21.99	28	22	29	18.69
ΣREE	88.26	87.08	88.52	80.51	78.62	80.15	81.77	99.81	90.77	116.77	118.83	98.83	109.15	66.80	56.12	107.88	101.94	–	–	–	–
LREE	74.35	73.09	74.51	67.83	65.76	67.38	69.21	83.46	75.47	97.01	98.89	81.91	90.78	54.91	46.41	89.99	85.61	–	–	–	–
HREE	13.91	14.00	14.00	12.68	12.86	12.77	12.56	16.35	15.30	19.76	19.94	16.92	18.37	11.89	9.71	17.89	16.33	–	–	–	–
LREE/HREE	5.34	5.22	5.32	5.35	5.12	5.28	5.51	5.10	4.93	4.91	4.96	4.84	4.94	4.62	4.78	5.03	5.24	–	–	–	–
La_N/Yb_N	5.65	5.84	5.93	6.11	5.74	5.73	6.14	5.07	4.93	4.69	4.92	4.74	4.98	4.89	5.16	5.39	5.65	–	–	–	–
δEu	1.11	1.08	1.08	1.02	1.20	1.14	1.19	1.03	0.97	1.01	1.00	1.00	0.76	1.12	1.10	1.02	1.09	–	–	–	–

CAB continental arc basalt

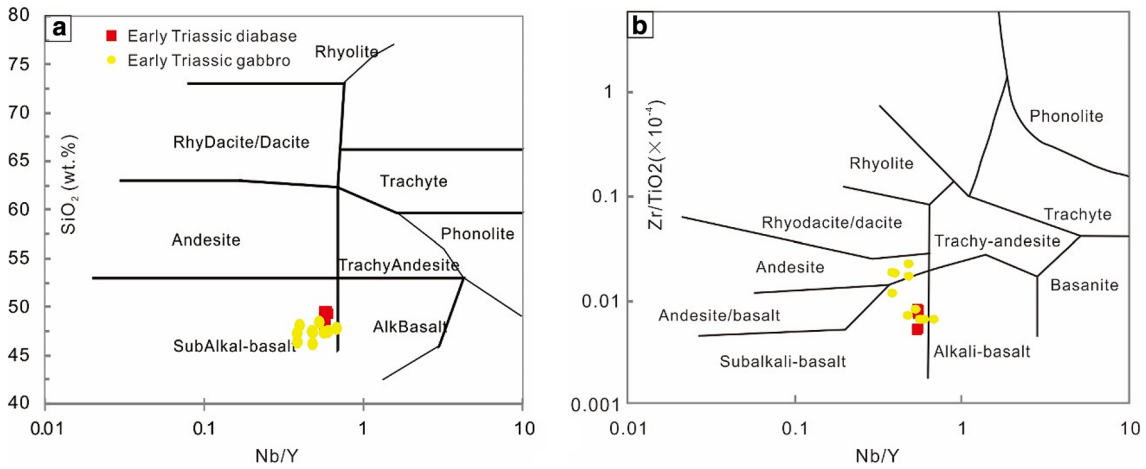

Fig. 6 Geochemical discrimination of the Early Triassic diabases and gabbros from the Rongma area in the northern margin of south Qiangtang. **a** Diagram of SiO_2 vs. Nb/Y (after Le Bas 2000); **b** diagram of Zr/TiO_2 ($\times 10^{-4}$) vs. Nb/Y (after Winchester and Floyd 1977)

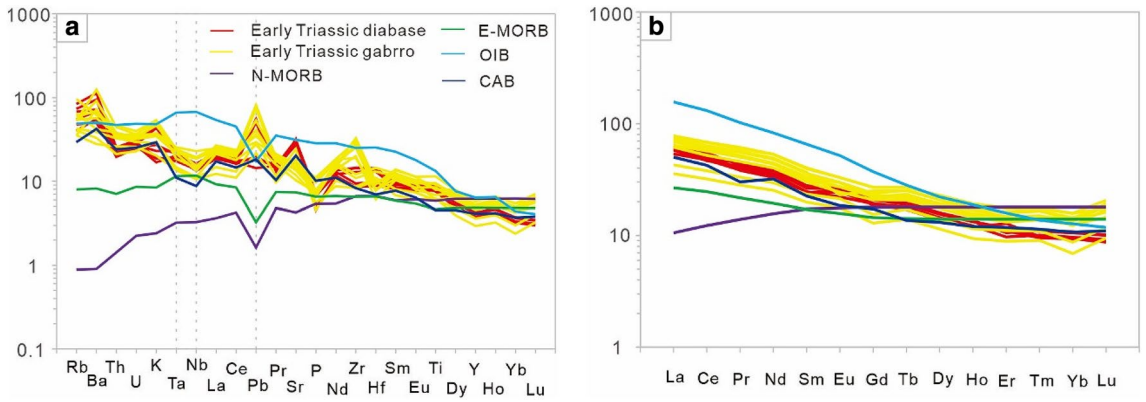

Fig. 7 **a** N-MORB-normalized trace element diagrams for the Early Triassic diabase and gabbro from the Rongma area in the northern margin of south Qiangtang. **b** chondrite-normalized REE diagram for the same mafic rocks as in a. The values of primitive mantle, OIB, N-MORB, and E-MORB are from Sun and McDonough (1989). The values of CAB are from Kelemen et al. (2007). The data of the Early Triassic diabase and gabbro in the Rongma area are from this study. OIB = island arc basalt, N-MORB = Normal mid ocean ridge basalt, E-MORB = Enriched mid ocean ridge basalt, CAB = continental arc basalt

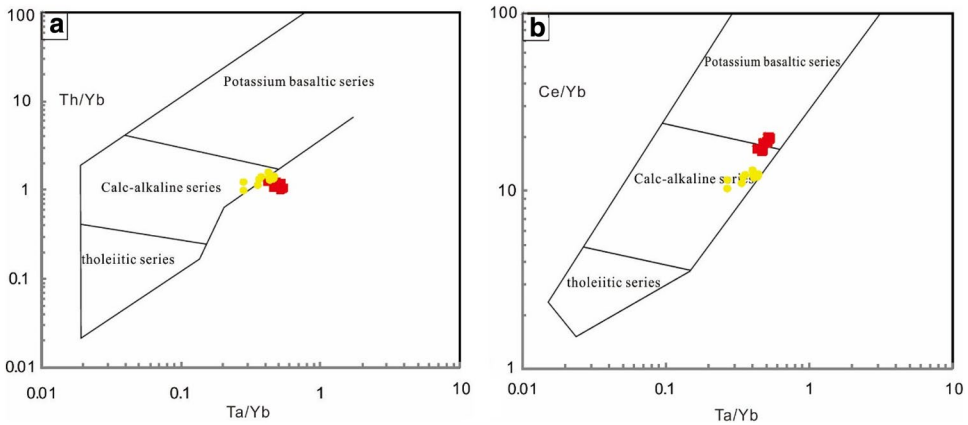

Fig. 8 Geochemical discrimination diagrams of magma series of diabase and gabbro from Rongma area in the northern margin of south Qiangtang. **a** Diagram of Th/Yb vs. Ta/Yb; **b** diagram of Ce/Yb vs. Ta/Yb. The symbols are the same as those in Fig. 6a

Table 4 Whole-Rock Nd isotopic compositions of the Early Triassic diabase from Rongma area in the northern margin of south Qiangtang

Sample No	Sm	Nd	$^{143}Nd/^{144}Nd < 2\delta >$	Age (Ma)	$^{147}Sm/^{144}Nd$	$(143Nd/144Nd)_i$	$\varepsilon_{Nd}(t)$	TDM
A1638-2	4.25	18.17	0.512513	241.2	0.145526	0.512283	− 0.9	1426
A1638-3	4.13	18.31	0.512506	241.2	0.140067	0.512285	− 0.8	1335
A1638-4	3.75	16.46	0.512504	241.2	0.141578	0.512281	− 0.9	1366
A1638-5	3.66	15.40	0.512514	241.2	0.147881	0.512280	− 0.9	1476

Table 5 Zircon Hf isotopic compositions of the Early Triassic diabase from Rongma area in the northern margin of south Qiangtang

No	Age (Ma)	$^{176}Yb/^{177}Hf$		$^{176}Lu/^{177}Hf$		$^{176}Hf/^{177}Hf$	2σ	$^{176}Hf/^{177}Hf_i$	$e_{Hf}(0)$	$e_{Hf}(t)$	T_{DM} (Ma)	$f_{Lu/Hf}$
A16138.2.1	241	0.0731	0.0008	0.0023	0.0000	0.282805	0.000035	0.282795	1.2	6.1	655	− 0.93
A16138.2.2	241	0.1279	0.0007	0.0037	0.0000	0.282820	0.000036	0.282803	1.7	6.4	660	− 0.89
A16138.2.3	241	0.2562	0.0027	0.0083	0.0000	0.282968	0.000033	0.282930	6.9	10.9	501	− 0.75
A16138.2.4	241	0.1072	0.0012	0.0032	0.0000	0.282784	0.000033	0.282769	0.4	5.2	706	− 0.90
A16138.2.5	241	0.1245	0.0019	0.0040	0.0001	0.282717	0.000026	0.282699	− 1.9	2.7	824	− 0.88
A16138.2.6	241	0.1545	0.0038	0.0044	0.0001	0.282933	0.000029	0.282913	5.7	10.3	498	− 0.87
A16138.2.7	241	0.1707	0.0034	0.0047	0.0001	0.282861	0.000029	0.282840	3.1	7.7	615	− 0.86
A16138.2.8	241	0.3642	0.0066	0.0122	0.0003	0.282876	0.000054	0.282821	3.7	7.0	759	− 0.63
A16138.2.9	241	0.1200	0.0009	0.0034	0.0000	0.282665	0.000029	0.282649	− 3.8	1.0	888	− 0.90
A16138.2.10	241	0.1232	0.0007	0.0033	0.0000	0.282839	0.000030	0.282824	2.4	7.1	624	− 0.90
A16138.2.11	241	0.1726	0.0004	0.0048	0.0000	0.282731	0.000029	0.282709	− 1.5	3.1	823	− 0.85
A16138.2.12	241	0.1690	0.0021	0.0047	0.0000	0.282777	0.000029	0.282756	0.2	4.7	747	− 0.86
A16138.2.13	241	0.1151	0.0008	0.0033	0.0000	0.282787	0.000027	0.282772	0.5	5.3	703	− 0.90
A16138.2.14	241	0.2173	0.0009	0.0075	0.0000	0.283175	0.000047	0.283141	14.2	18.3	131	− 0.77
A16138.2.15	241	0.1000	0.0002	0.0031	0.0000	0.282712	0.000026	0.282698	− 2.1	2.7	810	− 0.91
A16138.2.16`	241	0.1142	0.0008	0.0034	0.0000	0.282784	0.000022	0.282769	0.4	5.2	709	− 0.90
A16138.2.17	241	0.1816	0.0005	0.0051	0.0000	0.282629	0.000031	0.282606	− 5.1	− 0.6	991	− 0.85
A16138.2.18	241	0.1398	0.0005	0.0037	0.0000	0.282689	0.000029	0.282672	− 2.9	1.8	861	− 0.89
A16138.2.19	241	0.1165	0.0007	0.0033	0.0000	0.282735	0.000027	0.282721	− 1.3	3.5	781	− 0.90
A16138.2.20	241	0.1778	0.0028	0.0050	0.0001	0.282780	0.000029	0.282757	0.3	4.8	750	− 0.85
A16138.2.21	241	0.1999	0.0013	0.0064	0.0000	0.282898	0.000048	0.282869	4.5	8.7	586	− 0.81
A16138.2.22	241	0.1601	0.0020	0.0047	0.0000	0.283184	0.000043	0.283163	14.6	19.1	105	− 0.86
A16138.2.23	241	0.1146	0.0009	0.0033	0.0000	0.282864	0.000027	0.282850	3.3	8.0	585	− 0.90
A16138.2.25	241	0.1549	0.0007	0.0040	0.0000	0.282753	0.000036	0.282735	− 0.7	4.0	769	− 0.88
A16138.2.27	241	0.1640	0.0009	0.0045	0.0000	0.282675	0.000027	0.282654	− 3.4	1.1	903	− 0.86
A16138.2.28	241	0.1650	0.0006	0.0041	0.0000	0.282759	0.000035	0.282741	− 0.4	4.2	762	− 0.88
A16138.2.29	241	0.2373	0.0008	0.0068	0.0000	0.282780	0.000027	0.282749	0.3	4.5	792	− 0.79
A16138.2.30	241	0.2381	0.0012	0.0070	0.0000	0.282821	0.000030	0.282790	1.7	5.9	726	− 0.79
A16138.2.31	241	0.1656	0.0005	0.0044	0.0000	0.282827	0.000026	0.282808	2.0	6.6	662	− 0.87
A16138.2.32	241	0.1864	0.0007	0.0047	0.0000	0.282757	0.000033	0.282736	− 0.5	4.0	780	− 0.86
A16138.2.33	241	0.1681	0.0016	0.0047	0.0000	0.282813	0.000023	0.282791	1.4	6.0	692	− 0.86
A16138.2.34	241	0.1316	0.0005	0.0035	0.0000	0.282723	0.000030	0.282708	− 1.7	3.0	803	− 0.90
A16138.2.35	241	0.1723	0.0005	0.0045	0.0000	0.282702	0.000024	0.282682	− 2.5	2.1	861	− 0.86
A16138.2.36	241	0.1755	0.0008	0.0044	0.0000	0.282790	0.000033	0.282771	0.6	5.2	719	− 0.87
A16138.2.38	241	0.1609	0.0009	0.0041	0.0000	0.282681	0.000025	0.282663	− 3.2	1.4	882	− 0.88
A16138.2.39	241	0.2151	0.0008	0.0051	0.0000	0.282814	0.000034	0.282791	1.5	6.0	697	− 0.85

most regions. Spessartine isopleth have relatively steep slopes and their contents decrease with the increase of temperature. Because of the low content of pyrope in garnet core, there is a big error to define the P–T conditions of garnet core using the pyrope isopleth. Therefore, here we use the isopleth of spessartine and grossular content to define the P–T conditions of garnet core. The plot of chemical composition of garnet core indicates a P–T range

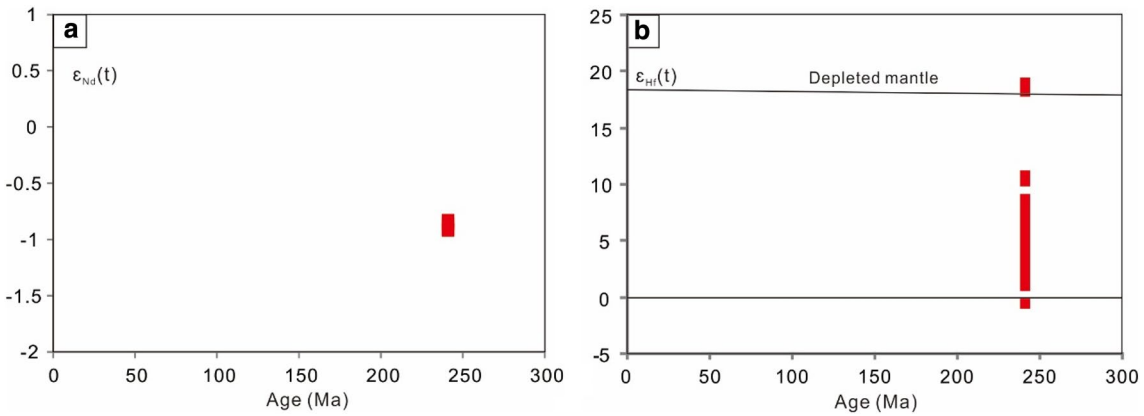

Fig. 9 **a** whole-rock $\varepsilon_{Nd}(t)$ vs. crystallization age of the early Triassic diabase from Rongma area in the northern margin of South Qiangtang; **b** zircon $\varepsilon_{Hf}(t)$ vs. zircon crystallization age of the early Triassic diabase in (**a**)

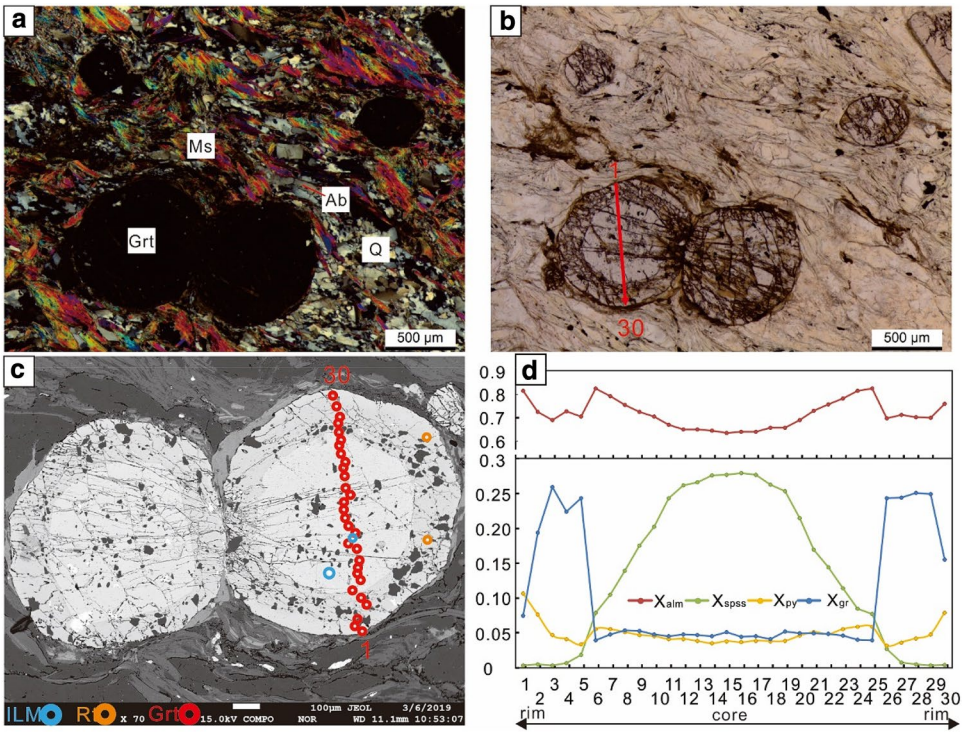

Fig. 10 Chemical composition of garnet of phengite–quartz schist from Rongma area in the northern margin of south Qiangtang. **a** cross-polarized light microscopic photo of phengite–quartz schist for microprobe analysis; **b** plane-polarized light microscopic photo of phengite–quartz schist for microprobe analysis; **c** BSE microscopic photo of garnet for microprobe analysis; **d** compositional profile of garnet. $X_{alm} = Fe^{2+}/(Fe^{2+} + Mn + Mg + Ca)$, $X_{py} = Mg/(Fe^{2+} + Mn + Mg + Ca)$, $X_{spss} = Mn/(Fe^{2+} + Mn + Mg + Ca)$, $X_{gr} = Ca/(Fe^{2+} + Mn + Mg + Ca)$. *Ab* albite, *Ms* Phengite, *Q* quartz, *Grt* garnet, *alm* almandine, *gr* grossular, *py* pyrope, *spss* spessartine

Table 6 Measured and effective whole-rock compositions of the garnet–phengite–quartz schist from Rongma area in the northern margin of south Qiangtang

Sample No	SiO_2	TiO_2	Al_2O_3	Fe_2O_3	FeO	MnO	MgO	CaO	Na_2O	K_2O	P_2O_5	LOI	Total
Measured whole-rock compositions													
7-29-3-b	67.43	1.01	14.57	0.78	6.21	0.16	1.73	0.50	1.32	2.94	0.10	2.44	99.18
	Si	Al	Fe3	Fe	Mn	Mg	Ca	Na	K	O			
Effective whole-rock compositions													
7-29-3-b	67.58	17.21	0.59	5.20	0.12	2.59	0.40	2.56	3.76	173.32			
	67.53	18.30	0.05	5.06	0.04	2.19	1.16	0.56	5.09	173.86			

Table 7 Garnet chemical composition of the garnet–phengite–quartz schist from Rongma area in the northern margin of south Qiangtang

	Sample	Min	SiO_2	TiO_2	Al_2O_3	Cr2O3	Fe_2O_3	FeO	MnO	MgO	CaO	Na2O	K2O	Totals	Oxygens	Si	Ti	Al	Cr	Fe3	Fe2	Mn	Mg	Ca	Na	K	Sum	A3	alm	spss	py	gr
	1.00	g	36.73	0.05	21.02	0.02	0.15	36.54	2.88	1.43	1.47	0.02	0.00	100.30	12.00	2.99	0.00	2.01	0.00	0.01	2.48	0.20	0.17	0.13	0.00	0.00	8.00	2.98	0.83	0.07	0.06	0.04
	2.00	g	37.36	0.12	20.89	0.01	0.00	35.75	0.13	2.01	3.83	0.06	0.01	100.15	12.00	3.01	0.01	1.98	0.00	0.00	2.41	0.01	0.24	0.33	0.01	0.00	8.00	2.99	0.81	0.00	0.08	0.11
	3.00	g	36.99	0.07	20.84	0.02	0.20	28.26	12.04	0.89	1.68	0.02	0.00	101.01	12.00	3.00	0.00	1.99	0.00	0.01	1.91	0.83	0.11	0.15	0.00	0.00	8.00	2.99	0.64	0.28	0.04	0.05
	4.00	g	38.10	0.14	21.26	0.00	0.00	31.95	0.14	1.20	8.43	0.03	0.01	101.25	12.00	3.01	0.01	1.98	0.00	0.00	2.11	0.01	0.14	0.71	0.01	0.00	7.99	2.98	0.71	0.00	0.05	0.24
Double zonation	5.00	g	37.34	0.03	21.04	0.02	0.00	36.11	0.13	2.65	2.57	0.00	0.01	99.91	12.00	3.01	0.00	2.00	0.00	0.00	2.43	0.01	0.32	0.22	0.00	0.00	7.99	2.98	0.82	0.00	0.11	0.07
	6.00	g	38.07	0.07	21.28	0.01	0.00	32.20	0.24	1.90	6.73	0.03	0.01	100.53	12.00	3.02	0.00	1.99	0.00	0.00	2.14	0.02	0.23	0.57	0.01	0.00	7.98	2.95	0.72	0.01	0.08	0.19
	7.00	g	37.66	0.10	20.97	0.03	0.00	30.41	0.14	1.15	8.92	0.03	0.00	99.41	12.00	3.02	0.01	1.99	0.00	0.00	2.04	0.01	0.14	0.77	0.00	0.00	7.98	2.96	0.69	0.00	0.05	0.26
	8.00	g	37.52	0.06	21.38	0.00	0.00	32.58	0.28	1.04	7.83	0.00	0.01	100.70	12.00	2.99	0.00	2.01	0.00	0.00	2.17	0.02	0.12	0.67	0.00	0.00	8.00	2.99	0.73	0.01	0.04	0.22
	9.00	g	37.80	0.14	21.27	0.00	0.00	31.36	0.81	0.84	8.43	0.04	0.00	100.69	12.00	3.01	0.01	2.00	0.00	0.00	2.09	0.05	0.10	0.72	0.01	0.00	7.99	2.96	0.71	0.02	0.03	0.24
	10.00	g	36.43	0.12	20.60	0.01	0.00	35.80	3.37	1.35	1.34	0.02	0.00	99.02	12.00	3.00	0.01	2.00	0.00	0.00	2.47	0.24	0.17	0.12	0.00	0.00	7.99	2.98	0.83	0.08	0.06	0.04
	11.00	g	36.84	0.02	20.83	0.00	0.00	34.66	4.55	1.36	1.62	0.06	0.01	99.95	12.00	3.00	0.00	2.00	0.00	0.00	2.36	0.31	0.17	0.14	0.01	0.00	8.00	2.98	0.79	0.11	0.06	0.05
	12.00	g	36.81	0.00	20.56	0.01	0.00	32.95	5.99	1.25	1.82	0.01	0.01	99.43	12.00	3.02	0.00	1.99	0.00	0.00	2.26	0.42	0.15	0.16	0.00	0.00	7.99	2.99	0.76	0.14	0.05	0.05
	13.00	g	37.06	0.03	20.93	0.01	0.00	31.70	7.57	1.16	1.80	0.03	0.01	100.28	12.00	3.01	0.00	2.00	0.00	0.00	2.15	0.52	0.14	0.16	0.00	0.00	7.99	2.97	0.72	0.18	0.05	0.05
	14.00	g	37.26	0.02	21.19	0.00	0.00	31.33	8.88	1.13	1.67	0.00	0.00	101.48	12.00	3.00	0.00	2.01	0.00	0.00	2.11	0.61	0.14	0.14	0.00	0.00	8.00	2.99	0.70	0.20	0.05	0.05
	15.00	g	37.15	0.07	21.04	0.05	0.02	29.80	10.70	1.02	1.58	0.00	0.00	101.44	12.00	2.99	0.00	2.00	0.00	0.00	2.01	0.73	0.12	0.14	0.00	0.00	8.00	3.00	0.67	0.24	0.04	0.05
	16.00	g	36.98	0.14	21.07	0.01	0.00	28.42	11.31	1.02	1.63	0.01	0.00	100.60	12.00	3.00	0.01	2.01	0.00	0.00	1.93	0.78	0.12	0.14	0.00	0.00	7.99	2.97	0.65	0.26	0.04	0.05
	17.00	g	36.78	0.26	20.93	0.02	0.00	28.07	11.36	0.93	1.58	0.06	0.00	99.99	12.00	3.00	0.02	2.01	0.00	0.00	1.91	0.78	0.11	0.14	0.01	0.00	7.99	2.95	0.65	0.27	0.04	0.05
	18.00	g	36.77	0.07	20.92	0.01	0.00	28.04	11.87	0.86	1.53	0.05	0.01	100.11	12.00	3.00	0.00	2.01	0.00	0.00	1.91	0.82	0.10	0.13	0.01	0.00	8.00	2.97	0.64	0.28	0.04	0.05
	19.00	g	37.09	0.04	20.86	0.00	0.00	27.91	12.05	0.94	1.75	0.07	0.00	100.72	12.00	3.01	0.00	1.99	0.00	0.00	1.89	0.83	0.11	0.15	0.01	0.00	8.00	2.99	0.63	0.28	0.04	0.05
	20.00	g	36.72	0.05	21.09	0.02	0.00	28.01	12.09	0.90	1.53	0.02	0.00	100.41	12.00	2.99	0.00	2.02	0.00	0.00	1.91	0.83	0.11	0.13	0.00	0.00	8.00	2.98	0.64	0.28	0.04	0.04
	21.00	g	37.37	0.10	21.15	0.01	0.00	28.08	11.99	0.96	1.55	0.03	0.00	101.25	12.00	3.01	0.01	2.01	0.00	0.00	1.89	0.82	0.12	0.13	0.01	0.00	7.98	2.96	0.64	0.28	0.04	0.05
	22.00	g	36.93	0.00	21.03	0.00	0.00	28.73	11.32	0.94	1.42	0.00	0.01	100.38	12.00	3.00	0.00	2.02	0.00	0.00	1.95	0.78	0.11	0.12	0.00	0.00	7.99	2.97	0.66	0.26	0.04	0.04
	23.00	g	36.46	0.01	20.58	0.00	0.15	28.49	10.87	0.94	1.77	0.02	0.03	99.32	12.00	3.00	0.00	2.00	0.00	0.01	1.96	0.76	0.12	0.16	0.00	0.00	8.00	2.99	0.66	0.25	0.04	0.05
	24.00	g	36.89	0.03	20.96	0.04	0.08	30.42	9.36	1.14	1.70	0.00	0.01	100.63	12.00	2.99	0.00	2.01	0.00	0.01	2.06	0.64	0.14	0.15	0.00	0.00	8.00	2.99	0.69	0.21	0.05	0.05
	25.00	g	37.13	0.11	21.03	0.02	0.00	32.21	7.38	1.27	1.71	0.05	0.02	100.94	12.00	3.00	0.01	2.00	0.00	0.00	2.18	0.50	0.15	0.15	0.01	0.00	8.00	2.98	0.73	0.17	0.05	0.05
	26.00	g	36.97	0.02	20.81	0.02	0.00	33.12	6.21	1.19	1.65	0.07	0.01	100.07	12.00	3.01	0.00	2.00	0.00	0.00	2.26	0.43	0.14	0.14	0.01	0.00	8.00	2.97	0.76	0.14	0.05	0.05
	27.00	g	37.10	0.00	21.10	0.01	0.25	34.77	5.01	1.38	1.60	0.00	0.00	101.22	12.00	2.99	0.00	2.01	0.00	0.02	2.34	0.34	0.17	0.14	0.00	0.00	8.00	2.99	0.78	0.11	0.06	0.05
	28.00	g	37.19	0.00	20.98	0.00	0.26	35.90	3.70	1.46	1.40	0.08	0.02	100.99	12.00	3.00	0.00	2.00	0.00	0.02	2.42	0.25	0.18	0.12	0.01	0.00	8.00	2.97	0.82	0.09	0.06	0.04
	29.00	g	37.29	0.00	21.43	0.04	0.00	36.05	3.34	1.44	1.34	0.05	0.01	100.99	12.00	3.00	0.00	2.03	0.00	0.00	2.43	0.23	0.17	0.12	0.01	0.00	7.99	2.94	0.82	0.08	0.06	0.04
	30.00	g	37.98	0.09	21.23	0.02	0.00	31.13	1.17	0.80	8.48	0.03	0.00	100.93	12.00	3.02	0.01	1.99	0.00	0.00	2.07	0.08	0.10	0.72	0.00	0.00	7.98	2.97	0.70	0.03	0.03	0.24
	31.00	g	37.77	0.11	21.45	0.01	0.00	31.99	0.35	0.93	8.58	0.01	0.00	101.20	12.00	3.00	0.01	2.01	0.00	0.00	2.12	0.02	0.11	0.73	0.00	0.00	8.00	2.98	0.71	0.01	0.04	0.24
	32.00	g	37.63	0.07	21.32	0.01	0.00	31.39	0.23	1.06	8.75	0.00	0.00	100.45	12.00	3.00	0.00	2.00	0.00	0.00	2.09	0.02	0.13	0.75	0.00	0.00	7.99	2.98	0.70	0.01	0.04	0.25
	33.00	g	37.88	0.09	21.19	0.00	0.00	31.31	0.14	1.21	8.71	0.00	0.01	100.54	12.00	3.01	0.01	1.99	0.00	0.00	2.08	0.01	0.14	0.74	0.00	0.00	7.99	2.98	0.70	0.00	0.05	0.25
	34.00	g	38.49	0.11	21.76	0.00	0.00	32.77	0.19	1.92	5.22	0.04	0.02	100.51	12.00	3.05	0.01	2.03	0.00	0.00	2.17	0.01	0.23	0.44	0.01	0.00	7.94	2.85	0.76	0.00	0.08	0.16
	35.00	g	36.71	0.10	20.42	0.01	1.07	36.12	0.08	2.33	2.69	0.04	0.01	99.58	12.00	2.99	0.01	1.96	0.00	0.07	2.46	0.01	0.28	0.23	0.01	0.00	8.00	2.98	0.82	0.00	0.09	0.08
	36.00	g	37.41	0.09	21.22	0.03	0.29	36.55	0.13	2.07	3.32	0.04	0.00	101.16	12.00	2.99	0.01	2.00	0.00	0.02	2.44	0.01	0.25	0.28	0.01	0.00	8.00	2.98	0.82	0.00	0.08	0.10
	37.00	g	37.89	0.13	21.40	0.00	0.00	31.77	0.11	1.31	8.27	0.05	0.00	100.93	12.00	3.00	0.01	2.00	0.00	0.00	2.11	0.01	0.16	0.70	0.01	0.00	7.99	2.97	0.71	0.00	0.05	0.24
	38.00	g	37.70	0.11	21.19	0.00	0.00	31.83	0.13	1.14	8.67	0.01	0.00	100.78	12.00	3.00	0.01	1.99	0.00	0.00	2.12	0.01	0.14	0.74	0.00	0.00	8.00	3.00	0.71	0.00	0.04	0.25
	39.00	g	37.64	0.12	21.18	0.00	0.00	31.80	0.18	1.03	8.76	0.00	0.00	100.70	12.00	3.00	0.01	1.99	0.00	0.00	2.12	0.01	0.12	0.75	0.00	0.00	8.00	3.00	0.71	0.00	0.04	0.25
	40.00	g	37.66	0.12	21.13	0.02	0.00	31.52	0.41	0.94	8.84	0.01	0.00	100.65	12.00	3.00	0.01	1.99	0.00	0.00	2.10	0.03	0.11	0.76	0.00	0.00	8.00	3.00	0.70	0.01	0.04	0.25

Table 7 (continued)

Sample	Min	SiO_2	TiO_2	Al_2O_3	Cr2O3	Fe_2O_3	FeO	MnO	MgO	CaO	Na2O	K2O	Totals	Oxygens	Si	Ti	Al	Cr	Fe3	Fe2	Mn	Mg	Ca	Na	K	Sum	A3	alm	spss	py	gr
41.00	g	37.43	0.09	21.19	0.01	0.00	31.05	1.51	0.86	8.15	0.02	0.00	100.31	12.00	3.00	0.01	2.00	0.00	0.00	2.08	0.10	0.10	0.70	0.00	0.00	8.00	2.99	0.70	0.03	0.03	0.23
42.00	g	37.16	0.06	20.95	0.01	0.00	36.05	3.55	1.26	1.69	0.01	0.00	100.73	12.00	3.01	0.00	2.00	0.00	0.00	2.44	0.24	0.15	0.15	0.00	0.00	7.99	2.98	0.82	0.08	0.05	0.05
43.00	g	36.75	0.01	21.04	0.00	0.45	34.11	5.25	1.36	1.64	0.00	0.00	100.60	12.00	2.98	0.00	2.01	0.00	0.03	2.31	0.36	0.16	0.14	0.00	0.00	8.00	2.98	0.78	0.12	0.06	0.05
44.00	g	36.87	0.07	20.86	0.03	0.00	31.73	8.31	1.11	1.55	0.00	0.00	100.53	12.00	3.00	0.00	2.00	0.00	0.00	2.16	0.57	0.14	0.14	0.00	0.00	8.00	3.00	0.72	0.19	0.05	0.05
45.00	g	37.20	0.10	21.09	0.01	0.00	30.13	9.87	1.01	1.68	0.00	0.01	101.09	12.00	3.00	0.01	2.01	0.00	0.00	2.03	0.68	0.12	0.15	0.00	0.00	7.99	2.98	0.68	0.23	0.04	0.05
46.00	g	37.27	0.10	20.84	0.00	0.05	30.43	9.53	1.02	1.87	0.07	0.00	101.17	12.00	3.01	0.01	1.98	0.00	0.00	2.05	0.65	0.12	0.16	0.01	0.00	8.00	2.99	0.69	0.22	0.04	0.05
47.00	g	36.53	0.05	20.72	0.00	0.45	29.63	9.92	1.02	1.71	0.00	0.01	100.03	12.00	2.99	0.00	2.00	0.00	0.03	2.03	0.69	0.12	0.15	0.00	0.00	8.00	2.99	0.68	0.23	0.04	0.05
48.00	g	36.85	0.10	20.89	0.01	0.00	29.29	10.45	0.97	1.64	0.01	0.00	100.21	12.00	3.00	0.01	2.01	0.00	0.00	2.00	0.72	0.12	0.14	0.00	0.00	7.99	2.98	0.67	0.24	0.04	0.05
49.00	g	36.83	0.06	20.72	0.03	0.00	29.83	10.23	1.02	1.54	0.02	0.00	100.26	12.00	3.00	0.00	1.99	0.00	0.00	2.03	0.71	0.12	0.14	0.00	0.00	8.00	3.00	0.68	0.24	0.04	0.05
50.00	g	37.02	0.02	21.00	0.01	0.00	29.81	10.45	1.02	1.56	0.00	0.00	100.90	12.00	3.00	0.00	2.01	0.00	0.00	2.02	0.72	0.12	0.14	0.00	0.00	8.00	2.99	0.67	0.24	0.04	0.05
51.00	g	36.62	0.04	20.78	0.00	0.53	29.27	10.37	1.07	1.62	0.01	0.02	100.32	12.00	2.99	0.00	2.00	0.00	0.03	2.00	0.72	0.13	0.14	0.00	0.00	8.00	2.98	0.67	0.24	0.04	0.05
52.00	g	36.71	0.03	20.67	0.00	0.32	30.61	9.18	1.11	1.59	0.01	0.00	100.22	12.00	3.00	0.00	1.99	0.00	0.02	2.09	0.63	0.14	0.14	0.00	0.00	8.00	3.00	0.70	0.21	0.05	0.05
53.00	g	37.09	0.05	21.01	0.00	0.27	30.25	9.72	1.05	1.80	0.02	0.01	101.27	12.00	2.99	0.00	2.00	0.00	0.02	2.04	0.66	0.13	0.16	0.00	0.00	8.00	2.99	0.68	0.22	0.04	0.05
54.00	g	36.88	0.05	20.66	0.01	0.43	30.85	8.76	1.16	1.70	0.04	0.01	100.53	12.00	3.00	0.00	1.98	0.00	0.03	2.10	0.60	0.14	0.15	0.01	0.00	8.00	2.99	0.70	0.20	0.05	0.05
55.00	g	36.71	0.01	20.77	0.03	0.51	32.60	6.69	1.27	1.78	0.00	0.00	100.37	12.00	2.99	0.00	1.99	0.00	0.03	2.22	0.46	0.15	0.16	0.00	0.00	8.00	2.99	0.74	0.15	0.05	0.05
56.00	g	37.25	0.00	20.93	0.00	0.00	34.26	5.72	1.34	1.47	0.01	0.00	100.98	12.00	3.01	0.00	1.99	0.00	0.00	2.31	0.39	0.16	0.13	0.00	0.00	8.00	2.99	0.77	0.13	0.05	0.04
57.00	g	36.72	0.03	20.84	0.00	0.18	36.16	3.29	1.21	1.61	0.05	0.00	100.08	12.00	3.00	0.00	2.00	0.00	0.01	2.47	0.23	0.15	0.14	0.01	0.00	8.00	2.98	0.83	0.08	0.05	0.05
58.00	g	37.60	0.05	20.99	0.01	0.00	31.14	0.70	0.83	8.98	0.03	0.00	100.34	12.00	3.01	0.00	1.98	0.00	0.00	2.08	0.05	0.10	0.77	0.01	0.00	8.00	3.00	0.69	0.02	0.03	0.26
59.00	g	37.77	0.12	20.89	0.00	0.00	31.62	0.33	0.92	8.80	0.05	0.00	100.50	12.00	3.02	0.01	1.97	0.00	0.00	2.11	0.02	0.11	0.75	0.01	0.00	8.00	3.00	0.70	0.01	0.04	0.25
60.00	g	37.67	0.08	21.08	0.01	0.00	31.72	0.26	0.95	8.62	0.01	0.00	100.40	12.00	3.01	0.01	1.99	0.00	0.00	2.12	0.02	0.11	0.74	0.00	0.00	7.99	2.99	0.71	0.01	0.04	0.25
61.00	g	37.46	0.11	20.89	0.03	0.33	31.23	0.12	1.08	8.96	0.03	0.00	100.24	12.00	3.00	0.01	1.97	0.00	0.02	2.09	0.01	0.13	0.77	0.01	0.00	8.00	3.00	0.70	0.00	0.04	0.26
62.00	g	37.99	0.17	21.09	0.00	0.00	33.30	0.13	1.50	6.81	0.06	0.00	101.04	12.00	3.02	0.01	1.98	0.00	0.00	2.21	0.01	0.18	0.58	0.01	0.00	7.99	2.98	0.74	0.00	0.06	0.19
63.00	g	37.70	0.04	21.15	0.03	0.00	37.17	0.12	2.34	2.51	0.03	0.02	101.11	12.00	3.01	0.00	1.99	0.00	0.00	2.48	0.01	0.28	0.22	0.00	0.00	7.99	2.98	0.83	0.00	0.09	0.07
64.00	g	37.62	0.04	21.22	0.00	0.00	36.43	0.09	2.58	2.60	0.02	0.00	100.60	12.00	3.01	0.00	2.00	0.00	0.00	2.44	0.01	0.31	0.22	0.00	0.00	7.99	2.97	0.82	0.00	0.10	0.08
65.00	g	36.98	0.00	21.01	0.01	0.63	35.21	4.25	1.37	1.59	0.05	0.00	101.11	12.00	2.98	0.00	2.00	0.00	0.04	2.38	0.29	0.17	0.14	0.01	0.00	8.00	2.97	0.80	0.10	0.06	0.05
66.00	g	37.72	0.13	21.28	0.00	0.00	36.84	0.12	2.71	2.47	0.00	0.00	101.26	12.00	3.00	0.01	2.00	0.00	0.00	2.45	0.01	0.32	0.21	0.00	0.00	7.99	2.99	0.82	0.00	0.11	0.07
67.00	g	37.01	0.07	20.82	0.00	0.45	28.50	11.39	1.06	1.88	0.00	0.00	101.17	12.00	2.99	0.00	1.98	0.00	0.03	1.93	0.78	0.13	0.16	0.00	0.00	8.00	2.99	0.64	0.26	0.04	0.05
68.00	g	37.31	0.00	21.07	0.02	0.13	36.30	3.23	2.07	1.07	0.00	0.00	101.19	12.00	3.00	0.00	2.00	0.00	0.01	2.44	0.22	0.25	0.09	0.00	0.00	8.00	3.00	0.81	0.07	0.08	0.03
69.00	g	37.43	0.06	21.29	0.00	0.00	31.02	0.86	1.02	8.36	0.01	0.00	100.06	12.00	3.00	0.00	2.01	0.00	0.00	2.08	0.06	0.12	0.72	0.00	0.00	7.99	2.98	0.70	0.02	0.04	0.24
70.00	g	38.14	0.11	21.33	0.07	0.00	31.41	0.10	1.23	8.61	0.01	0.00	101.01	12.00	3.02	0.01	1.99	0.00	0.00	2.08	0.01	0.15	0.73	0.00	0.00	7.98	2.96	0.70	0.00	0.05	0.25
71.00	g	37.25	0.09	21.21	0.00	0.30	32.11	0.15	1.49	7.46	0.03	0.01	100.09	12.00	2.99	0.01	2.01	0.00	0.02	2.15	0.01	0.18	0.64	0.00	0.00	8.00	2.98	0.72	0.00	0.06	0.21
72.00	g	37.02	0.06	20.66	0.00	0.36	36.21	0.16	2.77	2.21	0.04	0.00	99.49	12.00	3.00	0.00	1.98	0.00	0.02	2.46	0.01	0.33	0.19	0.01	0.00	8.00	2.99	0.82	0.00	0.11	0.06
73.00	g	37.26	0.06	20.94	0.01	0.00	34.34	0.23	2.12	4.65	0.04	0.03	99.67	12.00	3.01	0.00	1.99	0.00	0.00	2.32	0.02	0.26	0.40	0.01	0.00	8.00	2.99	0.77	0.01	0.09	0.13
74.00	g	37.92	0.05	21.29	0.00	0.00	33.66	0.11	1.82	5.69	0.03	0.00	100.56	12.00	3.02	0.00	2.00	0.00	0.00	2.24	0.01	0.22	0.49	0.00	0.00	7.98	2.95	0.76	0.00	0.07	0.16
75.00	g	37.71	0.18	21.24	0.03	0.00	33.84	0.18	2.05	5.65	0.00	0.01	100.90	12.00	3.00	0.01	1.99	0.00	0.00	2.25	0.01	0.24	0.48	0.00	0.00	7.99	2.99	0.75	0.00	0.08	0.16
76.00	g	37.79	0.12	21.23	0.00	0.00	30.95	0.18	1.44	8.40	0.03	0.04	100.17	12.00	3.01	0.01	2.00	0.00	0.00	2.06	0.01	0.17	0.72	0.01	0.00	7.99	2.96	0.70	0.00	0.06	0.24
77.00	g	37.53	0.11	21.04	0.02	0.00	31.98	0.33	1.11	8.08	0.04	0.01	100.24	12.00	3.01	0.01	1.99	0.00	0.00	2.14	0.02	0.13	0.69	0.01	0.00	8.00	2.99	0.72	0.01	0.04	0.23

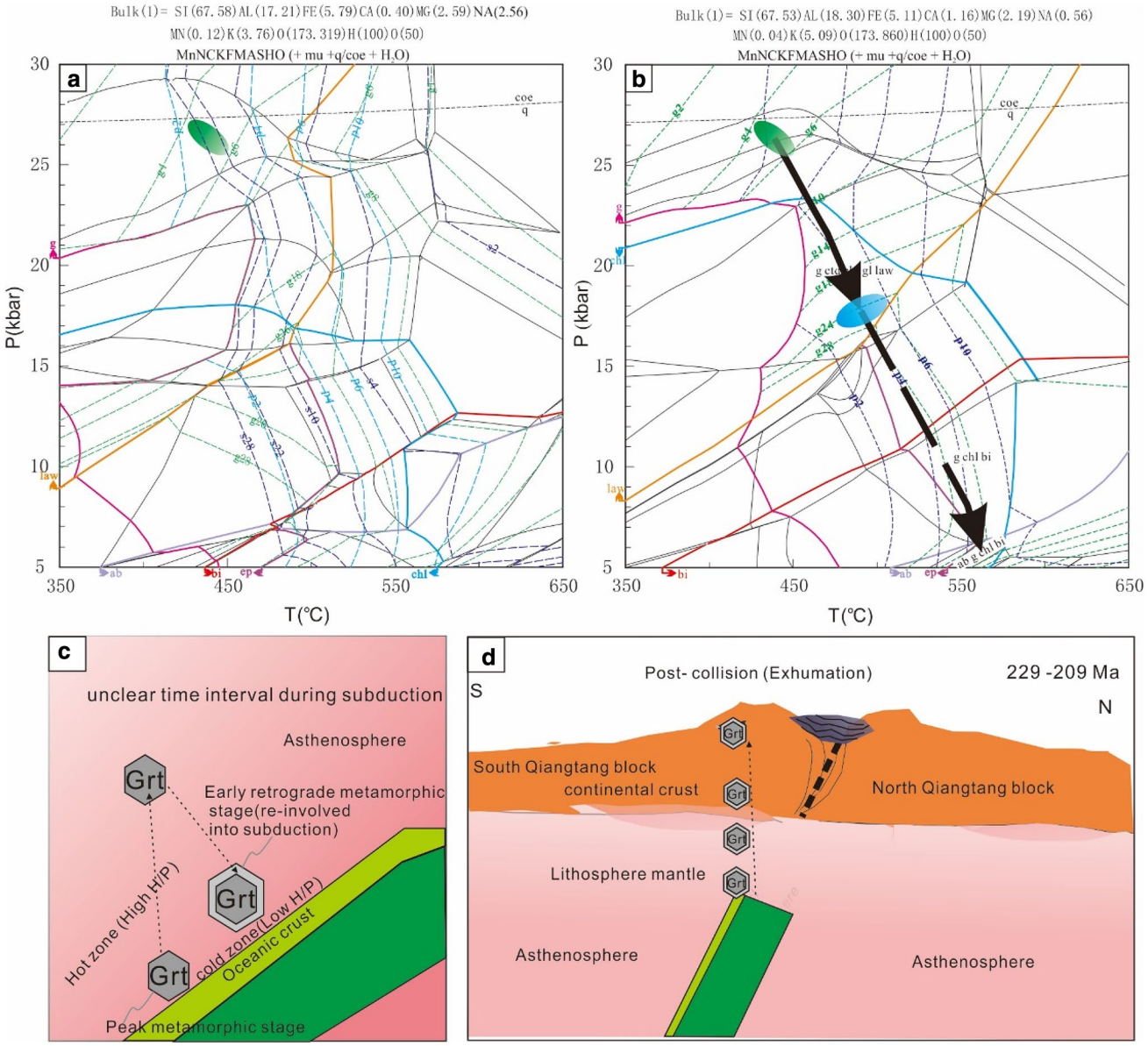

Fig. 11 Measured (**a**) and effective (**b**) P–T profile of garnet–phengite–quartz schist under MnNcKFMASHO system in Rongma area, in the northern margin of south Qiangtang. The apparent profile is calculated based on the measured (**a**) and effective (**b**) whole-rock composition in Table 6. In addition, the isopleth of spessartine content (e.g., blue dotted line s4), grossular content isopleth (e.g., green dotted line g28), and pyrope content isopleth (e.g., cyan dotted line p4) in garnet are also calculated. The green gradient shadow area represents the projection area of garnet core component, and the blue gradient shadow area represents the projection area of garnet edge component. The black thick solid line represents the metamorphic P–T path from the core to the edge of garnet, and the black thick dotted line represents the inferred partial late retrograde metamorphism path. Peak metamorphic stage mineral assemblages are garnet + phengite + quartz. The early retrograde metamorphic mineral assemblages are garnet + phengite + biotite + chlorite + quartz, and the late retrograde metamorphic mineral assemblages are garnet + phengite + biotite + chlorite + albite + quartz. (**c**–**d**) carton model of metamorphic process of garnet. It shows that garnet-phengite-quartz schist would be re-involved into subduction when its buoyant force was lower than the resultant of gravity and slab-pull forces. *alm* almandine, *ep* epidote, *gr* grossular, *law* andalusite, *py* pyrope, *spss* spessartine, *jd* jadeite, *ta* talc, *coe* coesite, *q* quartz, *hem* hematite, *chl* chlorite, *g* garnet, *ab* albite, *bi* biotite, *ph* phengite, *pl* plagioclase

of 25–27 kbar and 430–450 ℃ for the peak metamorphic stage (Fig. 11a).

P–T profile calculated using effective whole-rock composition by EPMA analysis and mineral volume content in MnNcKFMASHO system is shown in Fig. 11b. The phase diagram shows that garnet is stable in most areas and only disappears only at 350–460 ℃/5–22 kbar. Biotite is stable in the range of 370–650 ℃/5–16 kbar. Epidote is stable in

the range of 350–540 ℃/5–15 kbar. Andalusite is stable in the range of 350–630 ℃/14–30 kbar. Chlorite is stable in the range of 350–570 ℃/5–22 kbar. Albite is stable at 460–650 ℃/5–14 kbar. In addition, the isopleth of the contents of pyrope and grossular in garnet are also calculated. The phase diagram shows that isopleth of the pyrope contents has steep negative slopes, and its contents increase gradually with the increase of temperature. In the stable region of lawsonite, isopleth of the grossular contents have positive slopes and its content decreases gradually with the increase of pressure. In the stable region of epidote, isopleth of the grossular contents has steep negative slopes and its content gradually decreases with the increase of pressure. We can see that the isopleth of grossular and pyrope contents is only affected by pressure and temperature in the stable region of lawsonite, which can be used to define the formation conditions of garnet edge. The plot of chemical composition of garnet overgrowth rim indicates a P–T range of 17–19 kbar and 470–500 ℃ for the early retrograde metamorphic stage (Fig. 11b). However, the late retrograde metamorphic stage of T–P condition was not obtained.

Discussion

Metamorphic evolution of garnet–phengite–quartz schist

Based on petrographic observations, protoliths of garnet–phengite-quartz schist experienced at least three stages of metamorphic evolution (i.e., Peak metamorphic, early retrograde metamorphic, and late retrograde metamorphic stages). Model results indicate garnet core of garnet–phengite–quartz schist might form at depths of ~ 74–80 km (pressure gradient taking 0.03 GPa/km), whereas its overgrowth rim might experience burial to depths of 50–56 km. It also implies that the metamorphic evolution from core to overgrowth rim of garnet experienced a process of increasing temperature but decompression (Fig. 11b). Although the late retrograde metamorphic stage of T–P condition was not obtained, we infer that garnet–phengite–quartz schist exhumed to the upper crust or the surface with late retrograde metamorphism with cooling and decompression. The evolution path of increasing temperature but decompression from garnet core to overgrowth rim might respond to four complicated processes: (i) subduction—exhumation along subduction channel—involving subduction again—exhumation again; (ii) subduction—exhumation with magma emplacement and overgrowth of garnet core; (iii) crustal thickening—extensional exhumation with magma emplacement and overgrowth of the core, or (iv) subduction1exhumation—late hydrothermal alteration with overgrowth of garnet core. The garnet core domain shows a metamorphic characteristic with enrichment in spessartine and depletion in almandine which is distinct with magmatic garnet (duBray 1988; Dahlquist et al. 2007); thus, we exclude the two hypotheses of "ii" and "iii." Hydrothermal garnets would display obvious oscillating zonation (Clechenko and Valley 2003; Dziggel et al. 2009), while the garnet in this study does not have such characteristics of hydrothermal alteration. Hence, the hypothesis "iv" also be precluded and we infer that the evolution of garnet experienced a complicated process corresponding to hypothesis "i."

Obviously, the formation of garnet core should represent an earlier metamorphic event than its overgrowth rim. On the basis of the published data of the metamorphic rocks in the CQMB, different stages of metamorphism, such as eclogitic metamorphism subduction related of 230–244 Ma (Liang et al. 2017), were reported. Thus, we infer that the formation of garnet core might reflect early peak metamorphism related to deep subduction (~ 74–85 km), but growth rim of garnet might respond to early retrograde metamorphs related to re-involvement of subduction (50–56 km). As phengite has a closure temperature of ~ 350 ℃ and is a product of low-temperature, high-pressure metamorphism, it is usually formed in collisional orogenic belts (Jäger 1979). Consequently, we infer that ~ 227–225 Ma phengite age might reflect the late retrograde metamorphism related to exhumation after collision of Southern and Northern Qiangtang blocks. Then, how did the garnet–phengite–quartz schist exhume during the complicated subduction process? Due to garnet–phengite–quartz schist having lower density than eclogite, density difference between garnet–phengite–schist and meta-mafic rocks will increase with the increasing of subduction depth. This would result in the exhumation of schists along high-temperature low-pressure area (low-stress zone) in subduction channel (Wei et al. 2009). However, the meta-mafic rock blocks with higher density might continue to subduct into deeper mantle . In addition, compressive stress maintains in subduction channel during exhumation of garnet–phengite–quartz schist; thus, it will hinder the continuing exhumation of the schist. Hence, we infer that garnet–phengite–quartz schist would be re-involved into subduction when its buoyant force was lower than the resultant of gravity and slab-pull forces (Fig. 11c, d).

Formation and metamorphism time of metamorphic complexes

The U–Pb zircon dating results showed that the concordant ages of the zircon from the schist ranged from 393 to 2102 Ma, implying that the protolith of garnet–phengite–quartz schist deposited after 393 Ma. Metamorphic accreting rim occurred in the zircons of the schist, indicating that the protolith suffered from metamorphism, which surely occurred after 393 Ma. Abundant Precambrian ages,

including ~ 700 Ma, ~ 1000 Ma, ~ 1400 Ma, ~ 1800 Ma, and 2100 Ma, can be observed in the zircons of the schist (Table 1, Fig. 3d), suggesting Precambrian basements might exist in the region.

Two groups of phengite from the garnet–phengite–quartz schist yielded $^{40}Ar/^{39}Ar$ plateau ages of ~ 229 Ma and ~ 225 Ma, respectively (Fig. 5b, d), representing that the garnet–phengite–quartz schist was formed at ~ 229–225 Ma. As stated above, phengite is usually formed in collisional orogenic belts (Jäger 1979). Combined with regional dynamic evolution data (Table 8), the phengite $^{40}Ar/^{39}Ar$ plateau age of ~ 229–225 Ma obtained in this study most likely represented the time of regional exhumation after the collision of the Southern and Northern Qiangtang blocks.

Petrogenesis of mafic rocks

Given the relatively high LOI of early Triassic diabase and gabbro samples, some relatively stable elements, e.g., high field-strength elements (HFSEs) and SiO_2, are used to determine their petrogenesis. As shown in Fig. 12a, Nb/U ratios of mafic rocks do not show significant variation with LOI increase. On the whole-rock Zr/Y–Zr and Zr/TiO_2–Nb/Y diagrams (Fig. 6a, b), both seven diabase and eight gabbro samples fall into the sub-alkaline basalt field. Both the diabase and gabbro samples mainly show weak negative Nb, Ta, and Th, positive Pb anomalies, and low Nb/U (~ 13–24) and Ce/Pb (~ 3–11) ratios, with a right-inclined chondrite-normalized REE pattern, similar to average compositions of continental arc basalt (Kelemen et al. 2007) but distinct with OIB and MORB (Table 3, Fig. 7a, b). The Triassic diabase samples have $\varepsilon_{Nd}(t)$ of − 0.8 ~ 0.9, and zircon $\varepsilon_{Hf}(t)$ values of − 0.6 ~ 19.1. Two types of potential petrogenesis can be used to interpret these geochemical signatures: (i) the primary magma of diabase possibly is sourced from depleted mantle but suffered from contamination of minor crustal material, or (ii) the primary magma of diabase might be mainly sourced from enriched lithospheric mantle. Crustal contamination will increase abundance of SiO_2, Th/Nb, and lower Nb/U and $\varepsilon_{Nd}(t)$ (Cheng et al. 2018). However, on the Nb/U- SiO_2, $\varepsilon_{Nd}(t)$- SiO_2 and $\varepsilon_{Nd}(t)$- Nb/U diagrams (Fig. 12b-d), they showed opposite correlations, which indicates significant crustal contamination did not occur during formation of the diabase, and the primary magma of diabase might have formed by partial melting of enriched lithospheric mantle. In addition, similar whole-rock geochemical compositions between the diabase and gabbro samples indicate that they might have same petrogenesis related to the subduction of the Shuanghu Paleo-Tethys Ocean.

On the geochemical diagrams of the tectonic setting (Fig. 13a–f), both the early Triassic diabase and gabbro samples mainly fall into the intraplate extensional environment and display transition from OIB to MORB and arc basalt signatures; both the diabase and gabbro samples show weak depletion in HFSEs (e.g., Nb, Ta, and Th), suggesting that their primary magmas did not suffer from intense fluid metasomatism and crustal contamination. Thus, the diabase may have formed in a continental rift or back-arc extensional environment. Based on previous researches, regional metamorphism related to continent–continent collision occurred in the middle-late Triassic (227–209 Ma) (Zhai et al. 2009; Zhang et al. 2010; Zhu et al. 2010), with post-collision during ~ 225–200 Ma intervals (Wu et al. 2016; Xu et al. 2020; Zhu et al. 2010), suggesting that continental rift extension might occur after 200 Ma. In addition, ~ 244 Ma (Lu–Hf isochron age, Pullen et al. 2008) or ~ 237 Ma (U–Pb zircon age, Zhai et al. 2011b) eclogites related to northward subduction of the Shuanghu Paleo-Tethys Ocean were reported in the CQMB, which indicates a continental arc environment existed in the region during the early Triassic. Thus,

Table 8 The chronological data for the metamorphic complexes in the CQMB in the Central Qiangtang

Location	The name of the rock	Mineral	Age (Ma)	Data sources
Gangma Co	Garnet–Polysilica muscovite-schist	Polysilica muscovite	Ar–Ar (217.2 ± 1.8)Ma	Li et al. (2006)
Gangma Co	Garnet–Polysilica muscovite-schist	Polysilica muscovite	Ar–Ar 217.2–223.2 Ma	Zhai et al. (2009)
Gangma Co	Garnet–Polysilica muscovite-schist	Muscovite	Ar–Ar (213.2 ± 1.3)Ma	Zhang et al. (2010)
Qiangtang lanling	Garnet–Polysilica muscovite-schist	Polysilica muscovite	Ar–Ar 215-222 Ma	Li et al. (2006)
Qiangtang lanling	Blueschist	Polysilica muscovite	Ar–Ar 219.1–211.9 Ma	Liang et al. (2017)
Caiduo Caka, central Qiangtang	Blueschist	Glaucophane	Ar–Ar 209 ± 4 Ma	Zhu et al. (2010)
Rongma	Garnet–Polysilica muscovite-schist	Polysilica muscovite	Ar–Ar ~ 229–225 Ma	This article
Gangma Co	Eclogite	Polysilica muscovite	Ar–Ar ~ 214 Ma	Zhang et al. (2010)
Gangma Co	Eclogite	Zircon	U–Pb ~ 237–230 Ma	Zhai et al. (2011a, b)
Taoxinghu	Ophiolite	Zircon	U–Pb 467–460 Ma,	Li et al. (2008a)
Taoxinghu	Ophiolite	Zircon	U–Pb 505–517 Ma	Wu (2013)
Guoganjianianshan	Ophiolite	Zircon	U–Pb 438–431 Ma	Zhai et al. (2007)

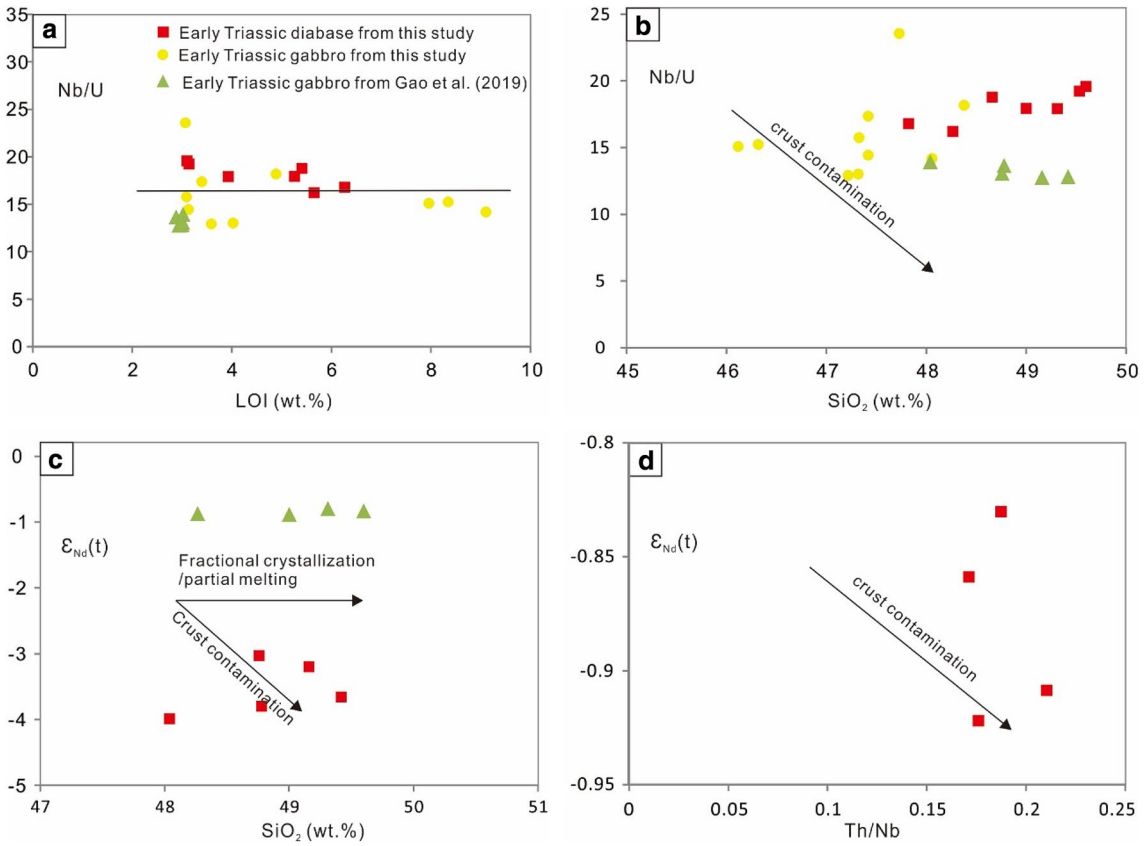

Fig. 12 Geochemical diagrams of the Early Triassic diabase and gabbro from Rongma area in the northern margin of south Qiangtang. **a** zircon ε_{Hf}(t) vs. crystallization age (*t*); **b** diagram of whole-rock $\varepsilon_{Nd}(t)$ vs. Ba/Th; **c** whole-rock $\varepsilon_{Nd}(t)$ vs. K_2O; **d** Ba/Th vs. Nb/U. Values of continental crust, BAB, OIB, N-MORB, and E-MORB are from Sun and McDonough (1989) and Gale et al. (2013)

a continental rift setting can be excluded in the northern margin of the Southern Qiangtang during the early Triassic. Consequently, combined with the whole-rock geochemical characteristics of the Early Triassic diabase and gabbro, we infer that they might form in a back-arc extensional setting, responding to the model of Zheng (2019).

Tectonic implications

The early Paleozoic ophiolitic mélange (e.g., Middle Ordovician ~ 467 Ma, Li et al. 2008a; Late Cambrian, ~ 517 Ma, Wu, 2013), including cumulate gabbro, plagiogranite, and basalt, was recognized along the CQMB and Geochemical data implies that they are characterized by N-MORB (Zhai et al. 2011a). Furthermore, Early Permian ophiolite (Li et al. 2008a, b) was also found in the LongmuTco–Shuanghu Suture Zone. In addition, the Late Carboniferous-Early Permian adakitic rocks and andesites related to subduction of Paleo-Tethys Oceanic were reported in the CQMB (Fig. 13a; Jiang et al. 2014; Zhang et al. 2014a, b). Therefore, the Paleo-Tethys Ocean might have been open since the Early Paleozoic and remained open in the Early Permian.

Many authors reported the Permo-Triassic arc-related igneous activity mainly in the Northern Qiangtang; thus, they interpreted these igneous rocks to be related to northward subduction of the Shuanghu Paleo-Tethys Ocean underneath the Northern Qiangtang (e.g., Zhang et al. 2006a, b; Zhai et al. 2011a, b; Li et al. 2019). However, some metamorphic rocks related to subduction of ocean plate were also recognized in the Southern Qiangtang (e.g., Liu et al. 2011; Zhu et al. 2015), favoring that view southward subduction of the Ocean underneath the Southern Qiangtang also occurring during the Early Triassic. In addition, recently Dan et al. (2020, 2021) reported abundant the Early Permian (~ 290–285 Ma)—Early Triassic (~ 239 Ma) mafic intrusions in the Southern Qiangtang block, and they proposed that the Early Permian mafic magmas were generated by a mantle plume, whereas the Early Triassic mafic rocks are derived from passive-margin magmatism caused by enhanced oceanic slab-pull forces. However, these mafic rocks show the geochemical features similar to continental arc basalt as the early Triassic mafic rocks in this study, such as low Nb/U (average on ~ 18) and Ce/Pb (average on ~ 9.6), weak–strong depletion in Nb and

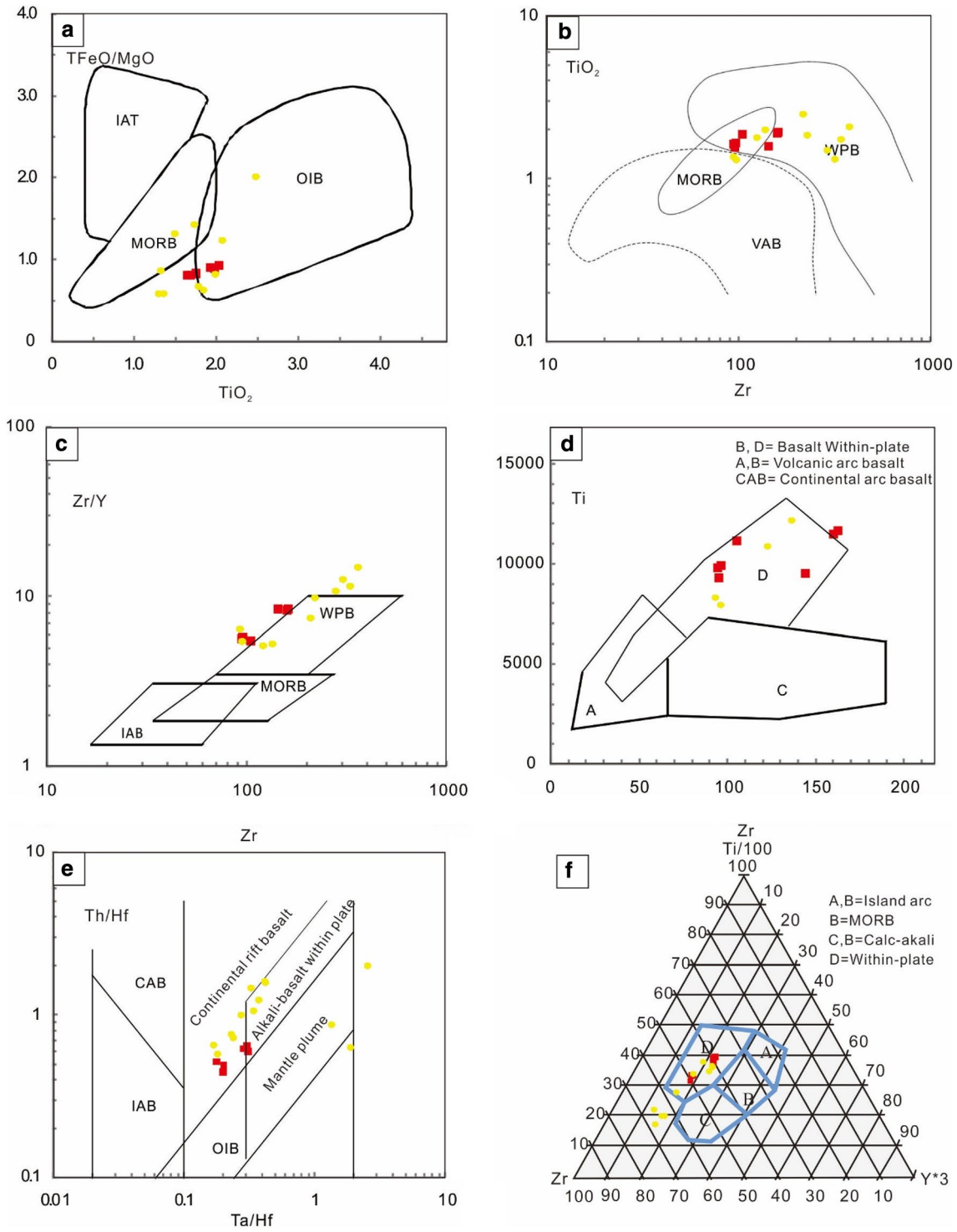

Fig. 13 Discrimination diagrams of the tectonic settings of the Early Triassic diabases and gabbros from the Rongma area, northern margin of south Qiangtang: **a** diagram of whole-rock TFeO/MgO vs. TiO_2; **b** diagram of whole-rock TiO_2 vs. Zr; **c** diagram of whole-rock Zr/Y vs. Zr (after Pearce and Norry 1979); **d** diagram of whole-rock Ti vs. Zr (after Pearce and Cann 1973); **e** diagram of whole-rock Th/Hf vs. Ta/Hf diagram (Zhang et al. 2004a, b, c), and **f** diagram of whole-rock Ti/100 vs. Zr vs. Y*3 (after Pearce and Cann 1973). The symbols are the same as those in Fig. 5a

Ta, and enrichment in Pb (Dan et al. 2020, 2021; Zheng 2019); hence, we infer these mafic rocks might form in a back-arc extensional setting caused by the subduction of the oceanic plate between the Northern and Southern Qiangtang blocks beneath the latter. Combined with the result from the metamorphic evolution of overgrowth zoning garnet from the schist in this study, we favor that view

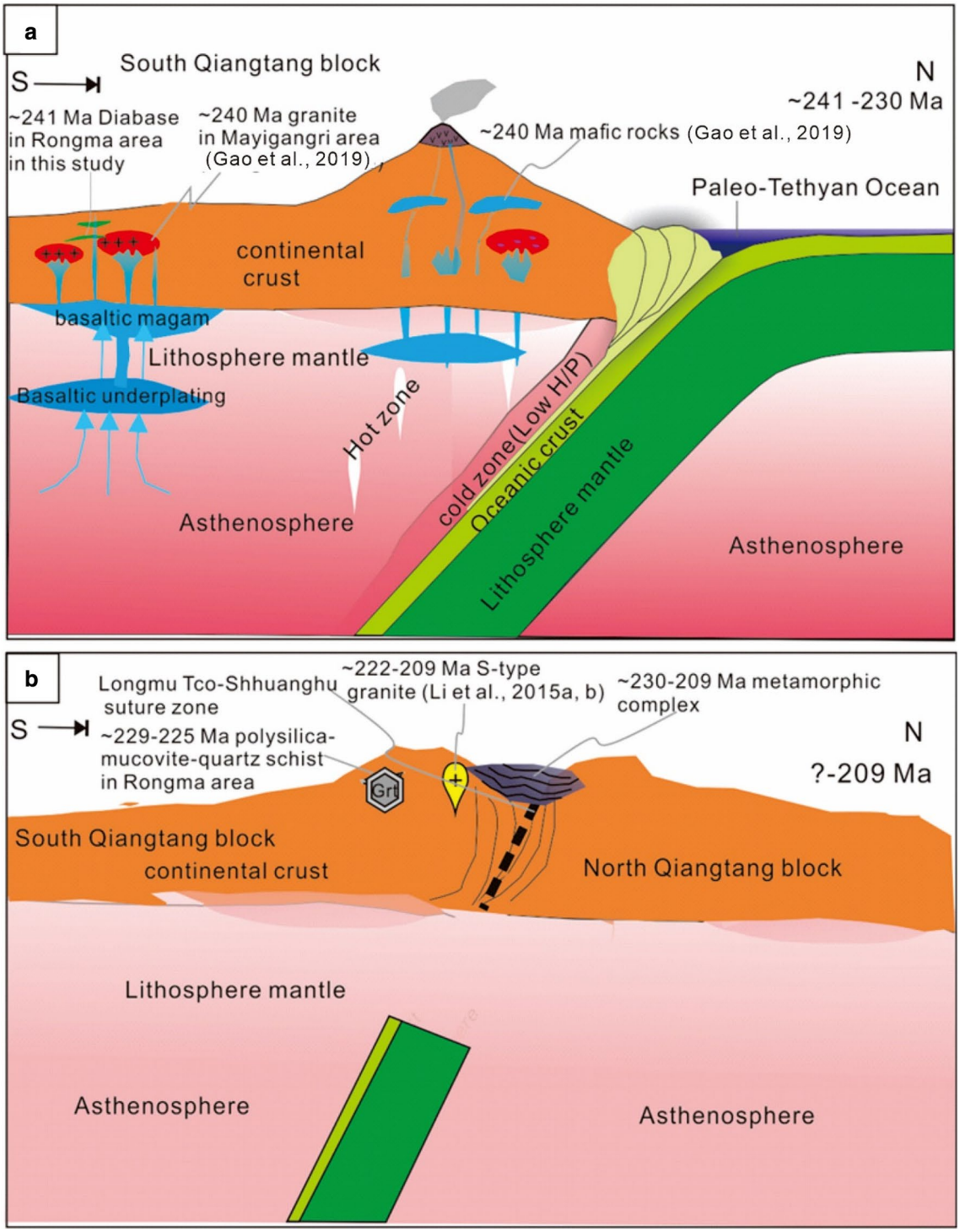

Fig. 14 Tectonic model of the Paleo-Tethys ocean in central Qiangtang during the Triassic Time. Chronological data of the metamorphic complex are shown in Table 8

bi-directional subduction of the Shuanghu Paleo-Tethys Ocean in the Early Triassic (Fig. 14a).

In addition, our Ar–Ar ages of phengites from the schist indicate the collision time of the two blocks might be earlier (> ~ 229 Ma). Combining with previous geochemical data, we propose that the Paleo-Tethys Ocean was finally closed at ~ 237– ~ 229 Ma, which is also consistent with some previous studies (e.g., Li et al. 2015a, b; Zhang and Tang 2009; Zhang et al. 2018). For instance, on the basis of previous Ar–Ar dating results of phengite from schists (Table 8), the collision of the southern and northern blocks with intense regional metamorphism had occurred before ~ 209 Ma, even tracing back to ~ 227 Ma. Li et al. (2015a, b) discovered simultaneous S-type granite in the Rongma area (222–210 Ma) (Fig. 14b), which also supported that the south and north Qiangtang blocks assembled in the late Triassic. In addition, Zhang et al. (2018) reported the Triassic Baqing eclogites across the CQMB in the north Qiangtang block, favored that the collision between the south and north Qiangtang blocks had occurred at ~ 223 Ma. Also, significant denudation occurred across the CQMB in temporal interval of 222–204 Ma (Zhang and Tang, 2009 and references therein). Thus, in this study we favor that the Paleo-Tethys Ocean had been open since the Early Paleozoic and remained open until the Early Triassic and was finally closed at ~ 237– ~ 229 Ma. This time model will help us better understand the tectonic evolution of the Paleo-Tethys Ocean.

Conclusions

(1) One diabase from the Rongma area yielded a zircon U–Pb age of 241.2 ± 1.1 Ma, one phengite–quartz schist yielded zircon-marginal concordant ages ranging from 1936 to 393 Ma, and two groups of phengite yielded Ar–Ar plateau ages of 229.0±1.4 Ma and 225.3±1.3 Ma, respectively. These ages indicate that the diabase was formed in the early Triassic, that sedimentation of the protolith of the garnet–phengite–quartz schist occurred after ~393 Ma, and that phengite formed in the Middle Triassic (~229 to 225 Ma).

(2) Whole-rock geochemistry of the early Triassic diabase and gabbro and whole-rock Nd and zircon-Hf isotopes of the diabase suggest that both the two early Triassic mafic rocks in the Rongma area are formed in a back-arc extensional setting.

(3) Chronological and geochemical evidence of the garnet–phengite–quartz schist and the early Triassic diabase and gabbro indicate that the Paleo-Tethys Ocean might be finally closed at ~237 to 229 Ma, and that the time of metamorphism of the phengite–quartz schist might respond to the exhumation of post-collision of the Southern and Northern Qiangtang blocks.

(4) Overgrowth zoning garnet in garnet–phengite–quartz schist with three stages of metamorphic evolution is recognized from garnet core to overgrowth rim, indicating two subduction in a short time might be involved its metamorphic evolution.

Acknowledgements This study is funded by China Geological Survey's project (No.KD-[2018]-XZ-035) 1:50000 Scale Regional Geological Survey of I45E022011 Mapsheet, South of Rongma Town, Tibet.

References

Andersen T (2002) Correction of common lead in U-Pb analyses that do not report 204 Pb. Chem Geol 192:59–79. https://doi.org/10.1016/S0009-2541(02)00195-X

Baldwin JA, Powell R, Brown M, Moraes R, Fuck RA (2005) Modelling of mineral equilibria in ultrahigh-temperature metamorphic rocks from the Anápolis-Itauçu Complex, central Brazil. J Metamorph Geol 23:511–531

Carson CJ, Powell R, Clarek GL (1999) Calculated mineral equilibria for eclogites in $CaO-Na_2O-FeO-MgO-Al_2O_3-SiO_2-H_2O$: application to the Poue´bo Terrane, Pam Peninsula, New Caledonia. J Metamorph Geol 17:9–24

Cheng ZG, Zhang ZC, Xie QH, Hou T, Ke S (2018) Subducted slab-plume interaction traced by magnesium isotopes in the northern margin of the Tarim Large Igneous Province. Earth Planet Sci Lett 489:100–110. https://doi.org/10.1016/j.epsl.2018.02.039

Coggon R, Holland TJB (2002) Mixing properties of phengitic micas and revised garnet-phengite thermobarometers. J Metamorph Geol 20(7):683–696

Dahlquist JA, Galindo C, Pankhurst RJ, Rapelad CW, Alasinoa PH, Saavedrae J, Fanning CM (2007) Magmatic evolution of the Peñón Rosado granite: Petrogenesis of garnet-bearing granitoids. Lithos 95:177–207

Dan W, Wang Q, White WM, Li XH, Zhang XZ, Tang GJ, Ou Q, Hao LL, Qi Y (2020) Passive-margin magmatism caused by enhanced slab-pull forces in central Tibet. Geology. https://doi.org/10.1130/G47957.1

Dan W, Wang Q, Murphy JB, Zhang XZ, Xu YG, White WM, Jiang ZQ, Ou Q, Hao LL, Qi Y (2021) Short duration of Early Permian Qiangtang-Panjal large igneous province: Implications for origin of the Neo-Tethys Ocean. Earth Planet Sci Lett 568:117054

Dziggel A, Wulff K, Kolb J, Meyer FM, Lahaye Y (2009) Significance of oscillatory and bell-shaped growth zoning in hydrothermal garnet: evidence from the Navachab gold deposit, Namibia. Chem Geol 262:262–276

de Capitani C, Petrakakis K (2010) The computation of equilibrium assemblage diagrams with Theriak/Domino software. Am Miner 95:1006–1016

Deng WM, Yin JX, Diao ZP (1996) The study on volcanic rocks and basic ultrabasic rocks in Chabu-Shuanghu area, Qiangtang. Sci China (series D) 26:296–301 (**in Chinese with English abstract**)

Diener JFA, Powell R, White RW, Holland TJB (2007) A new thermodynamic model for clino- and orthoamphiboles in the system $Na_2O-CaO-FeO-MgO-Al_2O_3-SiO_2-H_2O$. J Metamorph Geol 25:631–656

Du J, Zhang L, Shen X, Bader T (2014) A new P-T-t path of eclogites from Chinese southwestern Tianshan: constraints from

P-T pseudosections and Sm-Nd isochron dating. Lithos 200–201(258–27):2

Gale A, Dalton CA, Langmuir CH, Su Y, Schilling JG (2013) The mean composition of ocean ridge basalts. Geochem Geophys Geosyst 14:489–518. https://doi.org/10.1029/2012GC004334

Gao X, Li JC, Yuan GL, Wang GH, Liang X, Zheng YL, Wang Q (2019) Middle-Late Triassic magmatic records for the accretionary processes of South Qiangtang accretionary terrane: The mafic dykes in Mayigangri-Jiaomuri area, North Tibet. Acta Petrol Sin 35:760–774. https://doi.org/10.18654/1000-0569/2019.03.09

Green E, Holland T, Powell R (2007) An order-disorder model for omphacitic pyroxenes in the system jadeite-diopside-hedenbergite-acmite, with applications to eclogitic rocks. Am Miner 92:1181–1189

Holland T, Powell R (1998) An internally consistent thermodynamic data set for phases of petrological interest. J Metamorph Geol 16:309–343

Holland T, Powell R (2003) Activity-composition relations for phases in petrological calculations: an asymmetric multicomponent formulation. Contrib Miner Petrol 145:492–501

Hu PY, Li C, Li J, Wang M, Xie CM, Wu YW (2014) Zircon U-Pb–Hf isotopes and whole-rock geochemistry of gneissic granites from the Jitang complex in Leiwuqi area, eastern Tibet, China: Record of the closure of the Paleo-Tethys Ocean. Tectonophysics 623:83–99

Jäger E (1979) Introduction to geochronology. In: Lectures in isotope geology. Springer, Berlin, Heidelberg, pp 1–12

Jiang QY, Li C, Xie CM, Wang M, Hu PY, Wu H, Peng H, Chen JW (2014) Geochemistry and LA-ICP-MS zircon U-Pb age of volcanic rocks of Wangguoshan Formation in the Gangmar Co area of Qiangtang, Tibet. Geol Bull China 33:1702–1714 (**in Chinese with English abstract**)

Kapp P, Yin A, Manning CE, Murphy M, Harrison TM, Spurlin M, Ding L, Deng XG, Wu CM (2000) Blueschist-bearing metamorphic core complexes in the Qiangtang block reveal deep crustal structure of northern Tibet. Geology 28:19–22

Kapp P, Yin A, Manning CE, Harrison TM, Taylor MH, Ding L (2003) Tectonic evolution of the early Mesozoic blueschist-bearing Qiangtang metamorphic belt, central Tibet. Tectonics. https://doi.org/10.1029/2002TC001383

Kelemen PB, Hanghøj K, Greene AR (2007) One view of the geochemistry of subduction-related magmatic arcs, with an emphasis on primitive andesite and lower crust. Treatise Geochem 3:749–806

Le Bas M (2000) IUGS reclassification of the high-Mg and picritic volcanic rocks. J Petrol 41:1467–1470. https://doi.org/10.1093/petrology/41.10.1467

Li C (1987) The Longmu Co–Shuanghu–Lancangjiang plate suture and the north boundary of distribution of Gondwana affinity Permian–Carboniferous system in Northern Tibet, China. J Changchun Univ Earth Sci 17:155–166 (**in Chinese with English abstract**)

Li C, Cheng LR, Zhang YC, Zhai QG (2004) Discovery of Ordovician-Devonian strata in the south of the Qiangtang area, Tibet. Chin Sci Bull 23: 602–604 (**in Chinese with English abstract**)

Li C, Zhai QG, Cheng LR, Xu F, Huang XP (2005) Thought on some key geological problems in the Qiangtang area, Qinghai-Tibet Plateau. Geol Bull China 24:295–301 (**in Chinese with English abstract**)

Li C, Zhai QG, Chen W, Yu JJ, Huang XP, Zhang Y (2006) Ar-Ar chronometry of the eclogite from central Qiangtang area. Qinghai-Tibet Plateau. Acta Petrol Sin 22:2843–2849 (**in Chinese with English abstract**)

Li C, Zhai QG, Dong YS, Jiang GW, Jie C, Wu YW, Wang M (2008a) Oceanic crust on the northern margin of Gondwana-evidence from Early Paleozoic ophiolite in central Qiangtang, Qinghai-Tibet Plateau. Geol Bull China 27:1605–1612 (**in Chinese with English abstract**)

Li C, Zhai QG, Dong YS, Jiang GW, Xie CM, Wu YW, Wang M (2008b) Discovery of Eopaleozoic ophiolite in the Qiangtang of Tibet Plateau: evidence from SHRIMP U-Pb dating and its tectonic implications. Acta Petrol Sin 24:31–36 (**in Chinese with English abstract**)

Li GM, Li JX, Zhao JX, Qin KZ, Cao MJ, Evans NJ (2015a) Petrogenesis and tectonic setting of Triassic granitoids in the Qiangtang terrane, central Tibet: evidence from U-Pb ages, petrochemistry and Sr–Nd–Hf isotopes. J Asian Earth Sci 105:443–455

Li JC, Zhao ZB, Zheng YL, Yuan GL, Liang X, Wang GH, Liu X (2015b) The magmatite evidences in southern Qiangtang for Paleo-Tethys Ocean subducting collision: Gangtang-Co granites in Rongma, Tibet. Acta Petrol Sin 31:2078–2088 (**in Chinese with English abstract**)

Li S, Chung SL, Hou Z, Chew D, Wang T, Wang B, Wang Y (2019) Early mesozoic magmatism within the tibetan plateau: implications for the Paleo-Tethyan tectonic evolution and continental amalgamation. Tectonics 38:3505–3543

Liang X, Wang GH, Yang B, Ran H, Zheng YL, Du JX, Li LG (2017) Stepwise exhumation of the Triassic Lanling high-pressure metamorphic belt in Central Qiangtang, Tibet: insights from a coupled study of metamorphism, deformation, and geochronology. Tectonics 36:652–670. https://doi.org/10.1002/2016TC004455

Liu Y, Santosh M, Zhao ZB, Niu WC, Wang GH (2011) Evidence for palaeo-Tethyan oceanic subduction within central Qiangtang, northern Tibet. Lithos 127:39–53

Liu HY, Guo HM, Xing LN, Zhan YH, Li FL, Shao JL, Niu H, Liang X, Li CQ (2016) Geochemical behaviors of rare earth elements in groundwater along a flow path in the North China Plain. J Asian Earth Sci 117:33–51. https://doi.org/10.1016/j.jseaes.2015.11.021

Lu L, Zhang KJ, Yan LL, Jin X, Zhang YX (2017) Was Late Triassic Tanggula granitoid (central Tibet, western China) a product of melting of underthrust Songpan-Ganzi flysch sediments? Tectonics 36:902–928

Lu L, Qin Y, Li ZF, Yan LL, Jin X, Zhang KJ (2019) Diachronous closure of the Shuanghu Paleo-Tethys Ocean: constraints from the Late Triassic Tanggula arc-related volcanism in the East Qiangtang subterrane, Central Tibet. Lithos 328–329:182–199

Ludwig KR (2003) Isoplot/Ex, version 3.00: A geochronological toolkit for Microsoft Excel: Berkeley Geochronology Center Special Publication No. 4 Berkeley, California

Pearce JA, Cann JR (1973) Tectonic setting of basic volcanic rocks determined using trace element analyses. Earth Planet Sci Lett 19:290–300. https://doi.org/10.1016/0012-821X(73)90129-5

Pearce JA, Norry MJ (1979) Petrogenetic implications of Ti Zr, y, and Nb Variations in Volcanic Rocks. Contrib Mineral Petrol 69:33–47. https://doi.org/10.1007/BF00375192

Peng TP, Zhao GC, Fan WM, Peng BX, Mao YS (2015) Late Triassic granitic magmatism in the Eastern Qiangtang, Eastern Tibetan Plateau: geochronology, petrogenesis and implications for the tectonic evolution of the Paleo-Tethys. Gondwana Res 27:1494–1508

Pullen A, Kapp P, Gehrels GE (2008) Triassic continental subduction in central Tibet and Mediterranean-style closure of the Paleo-Tethys Ocean. Geology 36:351–354

Sun SS, McDonough WF (1989) Chemical and isotopic systematics of oceanic basalts: implications for mantle composition and processes. Geol Soc Lond Sp Pub 42:313–345. https://doi.org/10.1144/GSL.SP.1989.042.01.19

Tao Y, Bi XW, Li CS, Hu RZ, Li YB, Liao MY (2014) Geochronology, petrogenesis and tectonic significance of the Jitang granitic pluton in eastern Tibet, SW China. Lithos 184–187:314–323

Wang GH, Han FL, Yang YJ, Li YQ, Cui JL (2009) Discovery and geologic significance of late Paleozoic accretionary complexes in

central Qiangtang, northern Tibet, China. Chin Sci Bull 28:1181–1187 (**in Chinese with English abstract**)

Wang Q, Wang GH, Fang ZX, Wang H, Gao X (2019) Geochronology, geochemistry and tectonic significance of high-pressure metamorphic rocks from yadan area in central Qiangtang, Tibet. Acta Petrol Sin 35:775–798 (**in Chinese with English abstract**)

Wei CJ, Powell R, Clarke GL (2004) Calculated phase equilibria for low- and medium-pressure metapelites in the KFMASH and KMnFMASH systems. J Metamorph Geol 22:495–508

Wei C, Wang W, Clarke GL, Zhang L, Song S (2009) Metamorphism of high/ultrahigh-pressure pelitic–felsic schist in the South Tianshan Orogen, NW China: phase Equilibria and P–T path. J Petrol 50:1973–1991

White RW, Powell R, Holland TJB, Worley BA (2000) The effect of TiO2 and Fe2O3 on metapelitic assemblages at greenschist and amphibolite facies condition: mineral equilibria calculations in the system. J Metamorph Geol 18:497–511

White RW, Powell R, Holland TJB (2005) An in situ metatexite-diatexite transition in upper amphibolite facies rocks from Broken Hill, Australia. J Metamorph Geol 23:579–602

White RW, Powell R, Holland TJB (2007) Progress relating to calculation of partial melting equilibria for metapelites. J Metamorph Geol 25:511–527

Wilde SA, Zhou J-B (2015) The late Paleozoic to Mesozoic evolution of the eastern margin of the Central Asian Orogenic Belt in China. J Asian Earth Sci 113:909–921. https://doi.org/10.1016/j.jseaes.2015.05.005

Winchester JA, Floyd PA (1977) Geochemical Discrimination of Different Magma Series and Their Differentiation Products Using Immobile Elements. Chem Geol 20:325–343. https://doi.org/10.1016/0009-2541(77)90057-2

Wu YW (2013) The evolution record of Longmu Tco-Shuanghu-Lancang ocean: Cambrian-Permian ophiolites. Ph. D. Dissertation. Changchun: Jilin University, 1–162 (**in Chinese with English summary**)

Wu FY, Sun DY, Ge WC, Zhang YB, Grant ML, Wilde SA, Jahn BM (2011) Geochronology of the Phanerozoic granitoids in northeastern China. J Asian Earth Sci 41:1–30. https://doi.org/10.1016/j.jseaes.2010.11.014

Wu H, Li C, Chen J, Xie C (2016) Late Triassic tectonic framework and evolution of central Qiangtang, Tibet, SW China. Lithosphere 8:141–149

Xu W, Liu F, Dong Y (2020) Cambrian to Triassic geodynamic evolution of central Qiangtang, Tibet. Earth-Sci Rev 201:103083

Yin A, Harrison TM (2000) Geologic evolution of the Himalayan-Tibetan orogen. Annu Rev Earth Planet Sci 28:211–280. https://doi.org/10.1146/annurev.earth.28.1.211

Yu JJ, Wang F, Xu WL, Gao FH, Pei FP (2012) Early Jurassic mafic magmatism in the Lesser Xing'an–Zhangguangcai Range NE China, and its tectonic implications: constraints from Zircon U-Pb Chronology and Geochemistry. Lithos 142:256–266. https://doi.org/10.1016/j.lithos.2012.03.016

Zhai QG, Li C, Cheng LR, Zhang YC (2004) Geological features of Permian ophiolite in the Jiaomuri area, Qiangtang, Tibet, and its tectonic significance. Chin Sci Bull 23:1228–1230 (**in Chinese with English abstract**)

Zhai QG, Li C, Huang XP (2007) The fragment of Paleo-Tethys ophiolite from central Qiangtang, Tibet: geochemical evidence of metabasites in Guoganjianian. Sci China Ser D Earth Sci 50:1302–1309. https://doi.org/10.1007/s11430-007-0051-7

Zhai QG, Li C, Dong YS, Wang J, Chen W, Zhang Y (2009) Petrology, mineralogy and $^{40}Ar/^{39}Ar$ chronology for Rongma blueschist from central Qiangtang, northern Tibet. Acta Petrol Sin 25:2281–2288 (**in Chinese with English abstract**)

Zhai Q-G, Jahn M, Zhang RY, Wang J, Su L (2011a) Triassic subduction of the Paleo-Tethys in northern Tibet, China: evidence from the geochemical and isotopic characteristics of eclogites and blueschists of the Qiangtang Block. J Asian Earth Sci 42:1356–1370. https://doi.org/10.1016/j.jseaes.2011a.07.023

Zhai QG, Zhang RY, Jahn BM, Li C, Song SG, Wang J (2011b) Triassic eclogites from central Qiangtang, northern Tibet, China: petrology, geochronology and metamorphic P-T path. Lithos 125:173–189

Zhai QG, Jahn B, Su L, Wang J, Mo XX, Lee HY, Wang KL, Tang SH (2013) Triassic arc magmatism in the Qiangtang area, northern Tibet: zircon U-Pb ages, geochemical and Sr–Nd–Hf isotopic characteristics, and tectonic implications. J Asia Earth Sci 63:162–178

Zhang KJ, Tang XC (2009) Eclogites in the interior of the Tibetan Plateau and their geodynamic implications. Chin Sci Bull 54:2556–2567

Zhang CL, Ye HM, Wang AG, Guo KY, Dong YG (2004a) Geochemistry of the Neoproterozoic diabase and basalt in South of Tarim plate: evidence for the Neoproterozoic breakup of the Rodinia super-continent in south of Tarim. Acta Petrolog Sin 20:473–482 (**in Chinese with English abstract**)

Zhang YC, Li C, Cheng LR, Zhai QG (2004b) Discovery of Ordovician-Devonian strata in the south of the Qiangtang area, Tibet. Geol Bull China 23:602–604 (**in Chinese with English abstract**)

Zhang YC, Zhai QG, Li C, Cheng LR (2004c) Geological features of Permian ophiolite in the Jiaomuri area, Qiangtang, Tibet, and its tectonic significance. Geol Bull China 23:1228–1229 (**in Chinese with English abstract**)

Zhang KJ, Cai JX, Zhang YX, Zhao TP (2006a) Eclogites from central Qiangtang, northern Tibet (China) and tectonic implications. Earth Planet Sci Lett 245:722–729

Zhang KJ, Zhang YX, Li B, Zhu YT, Wei RZ (2006b) The blueschist-bearing Qiangtang metamorphic belt (northern Tibet, China) as an in situ suture zone: Evidence from geochemical comparison with the Jinsa suture. Geology 34:493–496

Zhang KJ, Zhang YX, Li B, Zhong LF (2007) Nd isotopes of siliciclastic rocks from Tibet, western China: Constraints on provenance and pre-Cenozoic tectonic evolution. Earth Planet Sci Lett 256:604–616

Zhang XZ, Dong YS, Li C, Chen W, Shi JRS, Zhang Y, Wang SY (2010) Identification of the eclogites with different ages and their tectonic significance in central Qiangtang, Tibetan Plateau: Constraints from ^{40}Ar-^{39}Ar geochronology. Geol Bull China 29:1815–1824 (**in Chinese with English abstract**)

Zhang KJ, Tang XC, Wang Y, Zhang YX (2011) Geochronology, geochemistry, and Nd isotopes of early Mesozoic bimodal volcanism in northern Tibet, western China: Constraints on the exhumation of the central Qiangtang metamorphic belt. Lithos 121:167–175

Zhang KJ, Zhang YX, Tang XC, Xia B (2012) Late Mesozoic tectonic evolution and growth of the Tibetan plateau prior to the Indo-Asian collision. Earth Sci Rev 114:236–249

Zhang L, Dong YS, Zhang XZ, Deng MR, Xu W (2014a) The discovery of the Early Permian adakitic rock in the Hongji Mountain area within central and western Qiangtang, Tibet Plateau, and its geological implications. Geol Bull China 33:1728–1739 (**in Chinese with English abstract**)

Zhang XZ, Dong YS, Li C, Deng MR, Zhang L, Xu W (2014b) Silurian high-pressure granulites from Central Qiangtang, Tibet: constraints on early Paleozoic collision along the northeastern margin of Gondwana. Earth Planet Sci Lett 405:39–51

Zhang XZ, Dong YS, Wang Q, Dan W, Zhang C, Deng MR, Wang X, Xia XP, Zeng JP, Liang H (2016) Carboniferous and Permian evolutionary records for the Paleo-Tethys Ocean constrained by

newly discovered Xiangtaohu ophiolites from central Qiangtang, central Tibet. Tectonics 35:1670–1686

Zhang YX, Jin X, Zhang KJ, Sun WD, Liu JM, Zhou XY, Yan LL (2018) Newly discovered Late Triassic Baqing Eclogite in Central Tibet indicates an anticlockwise West-East Qiangtang Collision. Sci Rep 8:966–966

Zhao Z et al (2015) Tectonic evolution and high-pressure rock exhumation in the Qiangtang terrane, central Tibet. Solid Earth 6:457–473

Zheng YF (2019) Subduction zone geochemistry. Geosci Front 10:1223–1254

Zhou JB, Wilde SA, Zhang XZ, Zhao GC, Zheng CQ, Wang YJ, Zhang XH (2009) The onset of Pacific margin accretion in NE China: evidence from the Heilongjiang high-pressure metamorphic belt. Tectonophysics 478:230–246. https://doi.org/10.1016/j.tecto.2009.08.009

Zhu TX, Zhang QY, Feng XT, Dong H, Yu YS, Li HR (2010) $^{40}Ar/^{39}Ar$ isotopic dating of the glaucophane in Caiduo Caka, Central Qiangtang area, northern Tibet, China, and its geological significance. Acta Geol Sin 84:1448–1456 (**in Chinese with English abstract**)

Zhu CY, Zhao G, Sun M, Liu Q, Han Y, Hou WZ, Zhang XR, Eizenhofer PR (2015) Geochronology and geochemistry of the Yilan blueschists in the Heilongjiang Complex, northeastern China and tectonic implications. Lithos 216:241–253. https://doi.org/10.1016/j.lithos.2014.12.021